

1                   **High-resolution thermal imaging in the Antarctic**  
2                   **marginal ice zone: Skin temperature heterogeneity and**  
3                   **effects on heat fluxes**

4                   **Ippolita Tersigni<sup>1</sup>, Alberto Alberello <sup>2</sup>, Gabriele Messori<sup>3,4</sup>, Marcello Vichi<sup>5,6</sup>,**  
5                   **Miguel Onorato<sup>7,8</sup>, and Alessandro Toffoli<sup>1</sup>**

6                   <sup>1</sup>Department of Infrastructure Engineering, The University of Melbourne, Parkville, VIC 3010, Australia

7                   <sup>2</sup>School of Mathematics, University of East Anglia, NR4 7TJ, Norwich, United Kingdom

8                   <sup>3</sup>Department of Earth Sciences and Centre of Natural Hazards and Disaster Science (CNDS), Uppsala  
9                   University, Uppsala, Sweden

10                  <sup>4</sup>Department of Meteorology and Bolin Centre for Climate Research, Stockholm University, Stockholm,  
11                  Sweden

12                  <sup>5</sup>Department of Oceanography, University of Cape Town, Cape Town, South Africa

13                  <sup>6</sup>Marine and Antarctic Research centre for Innovation and Sustainability, University of Cape Town, Cape  
14                  Town, South Africa

15                  <sup>7</sup>Dipartimento di Fisica, Università degli Studi di Torino, Via Pietro Giuria 1, 10125 Torino, Italy

16                  <sup>8</sup>INFN, Sezione di Torino, Via Pietro Giuria 1, 10125 Torino, Italy

17                   **Key Points:**

- 18                   • Thermal images of the ocean surface were used to compute heat fluxes over the  
19                   Antarctic marginal ice zone in winter and spring  
20                   • The marginal ice zone was a compound of several ice types with strong thermal  
21                   gradients in winter and more homogeneous temperature in spring  
22                   • The comparison of heat fluxes against reanalyses points towards biases due to the  
23                   skin temperature in winter and solar radiation in spring

---

Corresponding author: Ippolita Tersigni & Alessandro Toffoli, [ippolita.tersigni@gmail.com](mailto:ippolita.tersigni@gmail.com) &  
[toffoli.alessandro@gmail.com](mailto:toffoli.alessandro@gmail.com)

## Abstract

Insufficient in-situ observations from the Antarctic marginal ice zone limit our understanding and description of relevant mechanical and thermodynamic processes that regulate the seasonal sea ice cycle. Here we present high-resolution thermal images of the ocean surface and complementary measurements of atmospheric variables that were acquired underway during one austral winter and one austral spring expedition in the Atlantic and Indian sectors of the Southern Ocean. Skin temperature data and ice cover images were used to estimate the partitioning of the heterogeneous surface and calculate the heat fluxes to compare with ERA5 reanalyses. The winter marginal ice zone was composed of different but relatively regularly distributed sea ice types with sharp thermal gradients. The surface-weighted skin temperature compared well with the reanalyses due to a compensation of errors between the sea ice fraction and the ice floe temperature. These uncertainties determine the dominant source of inaccuracy for heat fluxes as computed from observed variables. In spring, the sea ice type distribution was more irregular, with alternation of sea ice cover and large open water fractions even 400 km from the ice edge. The skin temperature distribution was more homogeneous and did not produce substantial uncertainties in heat fluxes. The discrepancies relative to reanalysis data are however larger than in winter and are attributed to biases in the atmospheric variables, with the downward solar radiation being the most critical.

## Plain Language Summary

The Southern Ocean stores and release more heat than any other latitude band on the planet, making it a major element of the global climate. In the Antarctic, air-sea heat exchange is mediated by the seasonal sea ice cycle, which forms an unsteady and composite interface of several ice types. In-situ measurements are serendipitous in the region and models are poorly constrained. Here, we present a set of high-resolution thermal images of the uppermost ocean layer (skin temperature) and atmospheric variables acquired underway from the icebreaker S.A. Agulhas II in the austral winter and spring. Observations, and heat fluxes derived from them, are compared with reanalysis, which are model predictions adjusted with assimilated observations different from the ones we collected. In winter, the sea ice shows a neat separation between several ice types with sharp gradients of surface temperature. The reanalysis captures the mean skin temperature, but this is due to error compensation, which ultimately leads to inaccuracies in heat fluxes. In spring, sea ice is a disordered mixture of ice types and open water with a homogeneous thermal distribution. Uncertainties in skin temperature have smaller effects on the heat fluxes modelled by the reanalysis, and differences between reanalysis and observations are dominated by biases in solar radiation.

## 1 Introduction

The Southern Ocean is a major contributor to the global climate system (Huguenin et al., 2022). Its strong westerly winds fuel intense air-sea fluxes of momentum, energy, gas and freshwater at the ocean surface (e.g. Bharti et al., 2019; Landwehr et al., 2021). Forced by vigorous turbulent mixing through the Antarctic circumpolar current, energetic internal waves and some of the fiercest surface waves on Earth, these fluxes contribute to a deep mixed layer, which stretches from  $\approx 100$  m in the austral summer to  $\approx 500$  m in austral winter (Dong et al., 2008). This gives the Southern Ocean the capacity to store and release more energy than any other latitude band on the planet, with an annual average energy exchange capacity of  $\approx 30 \text{ Wm}^{-2}$  (Lytle et al., 2000). In comparison, the Arctic ocean has an average energy exchange of  $\approx 3 \text{ Wm}^{-2}$  (Krishfield & Perovich, 2005).

72 The energy balance combines the intake of shortwave radiation ( $Q_s$ ) originating  
 73 from the sun, the net longwave radiation ( $Q_b$ ), which is the difference between the down-  
 74 ward radiation from the atmosphere and the upwelling radiation from the ocean, and  
 75 the latent ( $Q_e$ ) and sensible ( $Q_h$ ) turbulent heat fluxes (Talley, 2011). At high latitudes,  
 76 the energy budget is complicated by the strong seasonal cycle of Antarctic sea ice (e.g.,  
 77 Dieckmann & Hellmer, 2010; Bourassa et al., 2013; Yu et al., 2017; Landwehr et al., 2021,  
 78 among others). By insulating the upper ocean from the lower atmosphere, sea ice en-  
 79 hances surface albedo, which changes from  $\approx 10\%$  in open water to  $\approx 20\%$  in young ice  
 80 to  $\approx 60\%$  in first year ice (Dieckmann & Hellmer, 2010). This fraction increases up to  
 81  $\approx 90\%$  in the presence of snow caps (Talley, 2011; R. A. Massom et al., 1998). The ab-  
 82 sorption of downward solar radiation varies strongly across the seasons. It exceeds  $200 \text{ Wm}^{-2}$   
 83 in an almost ice-free ocean during the austral summer and it drops by one order of mag-  
 84 nitude ( $Q_s \approx 10 \text{ Wm}^{-2}$ ) during autumn and winter (Yu et al., 2017).

85 The net longwave radiation depends primarily on the temperature of the upper-  
 86 most layer of the ocean surface (skin temperature; Talley, 2011), which has no heat ca-  
 87 pacity and, hence, responds instantaneously to changes in radiative (and turbulent) forc-  
 88 ing. As the upwelling radiation is generally greater than the downward counterpart, the  
 89 net radiation represents a loss of energy from the ocean with an annual average of  $\approx -50$   
 90  $\text{Wm}^{-2}$  across the Southern Ocean. The mixture of sea ice and open water fractions close  
 91 to freezing temperature in the Antarctic region produces a markedly colder ocean sur-  
 92 face, which enhances the net longwave radiation flux up to  $\approx 50\text{-}60\%$  relative to the an-  
 93 nual average (Yu et al., 2017).

94 The primary source of energy loss is represented by the latent and sensible fluxes,  
 95 which contribute to energy transfer through the evaporation of ocean water (or subli-  
 96 mation of sea ice) and the thermal vertical gradient between ocean and atmosphere, re-  
 97 spectively. The former is the dominant component during summer with an average of  
 98  $\approx -100 \text{ Wm}^{-2}$ , while sensible fluxes vary across zero as the thermal gradient is at its  
 99 minimum. During winter, the contribution of the latent flux eases (Yu et al., 2017). On  
 100 the contrary, the sensible flux grows, driven by a sharp thermal contrast (this is exac-  
 101 erbated in gaps between ice floes, leads in pack ice, water ponds and polynyas, where  $\Delta T$   
 102 can be up to  $\approx 20\text{-}40^\circ\text{C}$  during winter; Untersteiner, 1964), which enhances turbulent  
 103 mixing in the atmospheric boundary layer (Monin & Obukhov, 1954). Contributions can  
 104 be  $\approx -150 \text{ Wm}^{-2}$  (e.g. Kottmeier & Engelbart, 1992; Yu et al., 2017), making the sen-  
 105 sible fluxes the major component of energy loss during sea ice seasons (Lytle et al., 2000;  
 106 Yu et al., 2017). There is a significant regional variability across the Antarctic, though,  
 107 which is not well quantified yet (McPhee et al., 1996; Lytle et al., 2000).

108 Despite some observational evidence, dynamics of radiative and turbulent fluxes  
 109 remain elusive in the ice-covered ocean (Andreas et al., 2010; Bourassa et al., 2013), es-  
 110 pecially in the marginal ice zone (MIZ), i.e. the transition region of unconsolidated sea  
 111 ice that connects the ice-free sub-Antarctic with the Antarctic pack ice (e.g. Alberello  
 112 et al., 2019, 2022; Vichi et al., 2019; Vichi, 2022). Driven by atmospheric and oceanic  
 113 forcing (Gryschka et al., 2008; Vichi et al., 2019; Alberello et al., 2020; Womack et al.,  
 114 2022; Alberello et al., 2022), the MIZ is a mosaic of open water fragments and several  
 115 sea ice types, comprising of grease, frazil, pancakes, brash and compact ice, with vari-  
 116 able thickness of few tens of centimetres and concentration spanning 10-100% (e.g Al-  
 117 berello et al., 2019, 2022; Vichi, 2022; Brouwer et al., 2022). These inhomogeneities con-  
 118 tribute to a complicated distribution of the ocean skin temperature (e.g. R. Massom &  
 119 Comiso, 1994; Lytle et al., 2000; Bourassa et al., 2013), which is the single, most impor-  
 120 tant constraint for energy losses at high latitudes (Lytle et al., 2000; Zwally et al., 2002;  
 121 Dieckmann & Hellmer, 2010; Bourassa et al., 2013; Horvat & Tziperman, 2018).

122 A comprehensive figure of the sea ice fraction and skin temperature across the Antarc-  
 123 tic can be obtained by satellite remote sensing. Data are sampled over large footprints  
 124 of approximately  $25 \times 25 \text{ km}$  with temporal resolutions ranging from 12 to 48 hours. Al-

though large scale averages can be reliable (Fan et al., 2020), the coarse spatial and temporal resolutions are a source of uncertainty as they are not sufficient to detect the smaller spatial and sub-daily scale variability of the Antarctic MIZ (e.g. Kwok et al., 2003; Merchant et al., 2019; Vichi et al., 2019; Alberello et al., 2019, 2020; Womack et al., 2022). Furthermore, surface heterogeneity within the footprint produces signal noise (Rasmussen et al., 2018). Sensors are also susceptible to atmospheric properties such as cloud cover, which limits data availability (O’Carroll et al., 2019; Li et al., 2020). In-situ observations of sea ice concentration and surface temperature, which would underpin calibration and validation of remotely sensed products, are serendipitous in the Antarctic MIZ (Bourassa et al., 2013; Lytle et al., 2000; Skatulla et al., 2022), despite a large number of ship-based measuring campaigns taking place every year (Schmale et al., 2019).

The limited availability of in-situ data is also a challenge for the calibration and validation of numerical models and reanalysis products (Bourassa et al., 2013). Biases in energy fluxes are within  $\approx 10\text{--}40\text{ Wm}^{-2}$  (Yu et al., 2019) and escalate into uncertainties in sea ice thermodynamics and, hence, estimates of critical properties such as concentration and thickness (e.g. Rasmussen et al., 2018; Hall et al., 2015; Worby et al., 2008; Horvat, 2021). Interestingly, errors in shortwave and longwave radiations tend to cancel each other (Yu et al., 2019). Therefore, biases in the total energy budget are driven by uncertainties in turbulent fluxes (Liu et al., 2011).

Here we report in-situ measurements of sea ice concentration and surface temperature in the Antarctic MIZ during austral winter and spring. Observations were acquired using a high-speed and high-definition infrared (IR) camera, which captures the temperature of the uppermost (skin) surface layer and resolves the centimetre scale thermal inhomogeneity of the ocean surface (Fig. 1). Data are used to quantify the spatial variability of the sea ice concentration and skin temperature in the MIZ. Complemented by routine observations of atmospheric variables, thermal imaging is used to derive energy fluxes and assess effects of surface heterogeneity on the energy losses. Reanalysis data from the ERA5 archive (Hersbach et al., 2020) are compared against in-situ data to assess effects of small scale variance on key oceanic variables and uncertainties in energy fluxes.

## 2 Field measurements

In-situ measurements were conducted onboard the icebreaker S.A. Agulhas II, during two expeditions to the Antarctic MIZ in the Eastern Weddell Sea as part of the Southern Ocean Seasonal Experiment (SCALE 2019; Ryan-Keogh & Vichi, 2022). The first voyage took place in August 2019 to monitor the MIZ during its winter growth. The vessel, which set sail from Cape Town (South Africa), entered the MIZ at approximately  $56.5^{\circ}\text{S}$  and continued along the Greenwich meridian until consolidated sea ice was reached at a latitude of about  $58^{\circ}\text{S}$  ( $\approx 200\text{ km}$  from the ice edge; Fig. 1b). The vessel remained in sea ice for two days. The second voyage took place in October and November 2019 to survey the sea ice at the onset of its retreat phase. The vessel entered the MIZ at about  $55.8^{\circ}\text{S}$ , following a southward route. It reached consolidated sea ice at  $57.5^{\circ}\text{S}$  and continued until  $59^{\circ}\text{S}$  ( $\approx 300\text{ km}$  from the ice edge; Fig. 1c), before sailing eastwards to collect oceanographic and atmospheric data across a zonal sector spanning from  $0^{\circ}$  to  $24^{\circ}\text{E}$  (Fig. 1c). Overall, the spring expedition spent 12 days in sea ice.

Ocean surface characteristics were monitored with optical sensors. Surface wave properties and geometrical sea ice characteristics (e.g. floe size) were inferred through a stereo camera system in the visible range installed on the monkey island (details in Alberello et al., 2019, 2022). The skin temperature was surveyed with a *Telops* FAST-IR thermal imaging camera equipped with a 13 mm lens (angle of view of  $\approx 120^{\circ}$ ). To shield wind, rain and sea spray, it was mounted on an intermediate and less exposed deck at approximately 16 m above sea level. The camera was oriented port-side and inclined of

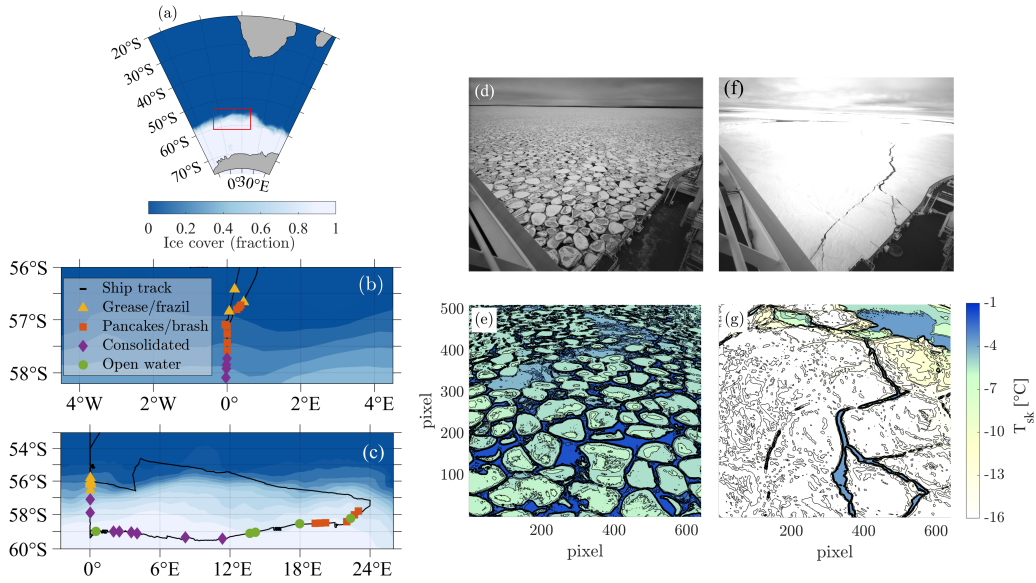


**Figure 1.** Overview of the expeditions and sample images: (a) Geographical location of the expeditions; (b,c) ship route in the MIZ with indication of monthly sea ice concentration (grading from blue for open waters to white for 100% concentration) and locations of the images and main representative sea ice types for the winter and the spring voyages; (d,e) sample images of pancake ice field in the visible and the infrared range, respectively (fields of view not collocated); (f,g) sample images of consolidated sea ice in the visible and the infrared range, respectively (fields of view not collocated). Sea ice concentration data in (a-c) are extracted from the Near-Real-Time NOAA/NSIDC Climate Data Record of Passive Microwave Sea Ice Concentration; sea ice types are from visual observations on board and from the image inspections.

176 approximately 40° relative to the horizon. The instrument acquired high-speed and high-  
 177 definition images in the mid-wave infrared range (MWIR, 3-5  $\mu\text{m}$ ) with a resolution of  
 178 640×512 pixels and at a minimum rate of 2 frames per second. Images were grouped in  
 179 20-minute sequences. Measurements were limited to a maximum of three sequences a day  
 180 in open waters, but were either continuous or hourly in the MIZ. Sample IR images with  
 181 the visible counterparts from other not co-located cameras are shown in Figs. 1d-g.

182 The IR sensor can detect surface temperature between  $-20$  and  $+45^\circ\text{C}$  with a de-  
 183 clared accuracy of  $\pm 0.005^\circ\text{C}$ . Calibration was performed by the manufacturer and cor-  
 184 recting coefficients were applied through an internal process. Performance was checked  
 185 in the laboratory before and after the expeditions by measuring the (known) temper-  
 186 ature of a black body. Image distortion due to the wide field of view of the lens was de-  
 187 tected during laboratory tests and rectified in post-processing.

188 The output image provided the skin temperature at each pixel, from which stan-  
 189 dard statistics such as the probability density function (pdf), related moments and ob-  
 190 servation ranges in the form of two times the standard deviation were derived for each  
 191 sequence. Furthermore, by relying on the freezing temperature, the open water fraction  
 192 was isolated and the sea ice concentration was estimated. The freezing temperature ( $T_f$ )  
 193 varied with salinity and it ranged from  $-1.86$  to  $-1.87^\circ\text{C}$  during the expeditions (cf. Millero,  
 194 1978). For the estimate of sea ice concentration, the median value of  $T_f = -1.865^\circ\text{C}$   
 195 was used. To avoid sample overlaps and to ensure the statistical independence of the records  
 196 only one thermal image every 10 seconds was selected. High humidity rates, haze, and  
 197 fog interfered with the infrared signal, returning unreliable temperature readings. IR im-  
 198 ages obtained during these conditions were excluded, noting that these conditions affected  
 199 primarily data in the open water. Overall, a total of 18 sequences were analyzed for the  
 200 winter expedition and 82 for the spring one. Despite the inclination of the camera, the  
 201 field of view still included records of surface temperature at far distances, the accuracy  
 202 of which is questionable. Hence, the analysis was confined to a window of 640×200 pix-  
 203 els, which coincides with the portion of image closer to the ship. The working window  
 204 defines a physical footprint of approximately 30×30 m, with a spatial resolution of roughly  
 205 0.05 m. A 20-minute sequence covered an overall swath of  $\approx 30\text{ m} \times 3\text{ km}$ .

206 The data set was complemented with standard atmospheric variables, including wind  
 207 speed, air temperature, saturated and specific humidity, and solar radiation through the  
 208 photosynthetically active radiation (PAR). These were acquired underway from the au-  
 209 tomatic met-station, which was operated by the South African Weather Service (Ryan-  
 210 Keogh & Vichi, 2022). Furthermore, sea ice temperature was retrieved from cores ex-  
 211 tracted at a few stations in the MIZ (Omatuku Ngongo et al., 2022; Audh et al., 2022;  
 212 Skatulla et al., 2022; S. Johnson et al., 2023). Samples were taken directly from undis-  
 213 turbed compact sea ice and from pancakes lifted onto the ship deck. Temperature was  
 214 measured immediately after coring, to minimise alterations. Routine visual observations  
 215 of sea ice (Hepworth et al., 2020), including concentration and type, were recorded fol-  
 216 lowing the Antarctic Sea Ice Processes and Climate (ASPeCt) protocol (Worby & Comiso,  
 217 2004), throughout the time spent in the MIZ.

### 218 3 Computation of surface energy fluxes

219 There are several empirical formulae for estimating surface energy fluxes. Herein,  
 220 those proposed in Talley (2011) are used.

221 The downward shortwave (solar) radiation ( $Q_{s_d}$ ) was measured as PAR on the ship  
 222 and estimated following the method in McCree (1972). The portion of solar radiation  
 223 absorbed by the ocean surface is computed as

$$Q_s = Q_{s_d}(1 - \alpha), \quad (1)$$

224 where  $\alpha$  is the albedo of the individual surface components (ocean and sea ice) extrap-  
 225 olated from Table 5 in Brandt et al. (2005) as a function of season, latitude and longi-  
 226 tude.

227 The net longwave radiation is calculated as

$$Q_b = \epsilon\sigma_{SB}T_{sk}^4(0.39 - 0.05e^{1/2})(1 - kC^2) + 4\epsilon\sigma_{SB}T_{sk}^3(T_{sk} - T_A), \quad (2)$$

228 where  $\epsilon = 0.98$  is the emittance of sea surface (Talley, 2011);  $\sigma_{SB} = 5.6687 \times 10^{-8} \text{ Wm}^{-2}\text{K}^{-4}$   
 229 is the Stefan-Boltzmann constant;  $T_{sk}$  and  $T_A$  are the ocean skin and air temperature,  
 230 respectively;  $k = 0.67-0.75$  is a latitude-dependent cloud cover coefficient (J. H. John-  
 231 son et al., 1965);  $C$  is the fractional cloud cover, which was derived from collocated satel-  
 232 lite observations as it was not measured directly; and  $e$  is the water vapor pressure, which  
 233 is the product of saturated vapor pressure ( $e_s$ ) and the relative humidity (RH; Bechtold,  
 234 2009). Values for  $e_s$  are determined as (Buck, 1981)

$$e_s = 6.1121 \exp \left[ \left( 18.678 - \frac{T_A}{234.5} \right) \left( \frac{T_A}{257.14 + T_A} \right) \right] \quad (3)$$

235 in open water and

$$e_s = 6.1115 \exp \left[ \left( 23.036 - \frac{T_A}{333.7} \right) \left( \frac{T_A}{279.82 + T_A} \right) \right] \quad (4)$$

236 in sea ice.

237 The latent heat flux ( $Q_e$ ) is estimated as

$$Q_e = \rho L C_e u (q_s - q_a), \quad (5)$$

238 where  $L$  is the latent heat of evaporation in open water ( $2260 \text{ KJ kg}^{-1}$ ) and sublima-  
 239 tion in sea ice ( $2838 \text{ KJ kg}^{-1}$ );  $\rho = 1.3 \text{ kg m}^{-3}$  is the average air density;  $u$  is the wind  
 240 speed;  $q_s$  is the saturated specific humidity at the surface temperature; and  $q_a$  is the spe-  
 241 cific humidity. It is assumed that turbulent mixing does not change with height in the  
 242 atmospheric boundary layer. Therefore, the transfer coefficient for latent heat  $C_e$  is set  
 243 as a vertically invariant scaling parameters, which is defined as  $C_e = 1.20 \times 10^{-3}$  (Smith,  
 244 1988). An alternative approach to evaluate  $C_e$  refers to the roughness lengths of momen-  
 245 tum, temperature and moisture (see e.g. Andreas et al., 2010; Biri et al., 2023). Rela-  
 246 tive to the vertical invariant scaling, though, this latter approach does not lead to sig-  
 247 nificantly different values (see Appendix A).

248 The sensible heat flux ( $Q_h$ ) is computed as

$$Q_h = \rho c_p C_h u (T_{sk} - T_A), \quad (6)$$

249 where  $c_p = 1004 \text{ KJ kg}^{-1} \text{ K}^{-1}$  is the specific heat capacity of air at constant pressure.  
 250 With a vertically invariant scaling approach, the transfer coefficient for sensible heat is  
 251 expressed as  $C_h = 1.0 \times 10^{-3}$  (Talley, 2011).

252 As the ocean in the MIZ is a composite of two main surfaces, the fluxes were com-  
 253 puted separately for sea ice and open water partitions (the mosaic approach; Andreas  
 254 et al., 2010). The overall flux emerging from the heterogeneous surface is estimated through  
 255 a weighted average, where the weight is expressed as a function of the sea ice concen-  
 256 tration  $C_i$ . For a generic component of the energy budget (labeled as  $Q_g$ ), the result-  
 257 ing flux is expressed as:

$$Q_g = C_i(Q_g)_{ice} + (1 - C_i)(Q_g)_{water}. \quad (7)$$

258 The total heat flux ( $Q_T$ ) at the ocean surface is the sum of all radiative and tur-  
 259 bulent fluxes:

$$Q_T = Q_s + Q_b + Q_e + Q_h. \quad (8)$$

## 4 In-situ sea ice observations from IR images

### 4.1 Reliability of skin temperature from IR images

The skin temperature from IR images was tested against satellite data and core measurements. In the the open ocean, the benchmark skin temperature was retrieved from several satellite-borne sensors available through the Near-Real-Time NOAA/NSIDC Climate Data Record of Passive Microwave Sea Ice Concentration database (Chin et al., 2017). Collocation was enforced by clustering and averaging the data over grids with side of 0.25 degrees and centered on ship’s positions; a 50% overlap between consecutive locations was considered. In the MIZ, only the skin temperature of the sea ice fraction was considered and it was compared against co-located measurements of near-surface temperature from ice cores (see §2). Co-located observations of sea ice skin temperature from satellite-born infrared sensors were not available due to cloud cover.

The data comparison is presented in Fig. 2. Observation ranges, shown in the form of errors bars, were small (and hidden by the symbols) for the open ocean measurements, indicating a homogeneous distribution of skin temperature in the grid box. An evident variability was found in the MIZ, denoting a more heterogeneous temperature distribution of sea ice (see §4.2).

The open ocean skin temperature from the IR camera was in good quantitative agreement with satellite sensors. The sea ice skin temperature was also consistent with ice core measurements. However, there is an evident bias, yet confined within the observation range, with the IR camera returning a colder surface temperature. Whereas the camera detects the uppermost surface layer, the ice core measurements refer to a less exposed and, hence, warmer sub-layer.

### 4.2 Skin temperature and sea ice concentration

The bulk weighted average of the skin temperature from the IR images is presented in Figs. 3 and 4 as a function of time and distance from the ice edge for winter and spring, respectively. The weighted average mediates sea ice and open water partitions and is computed as:

$$T_{sk} = C_i(T_{sk})_{ice} + (1 - C_i)(T_{sk})_{water}, \quad (9)$$

where  $(T_{sk})_{ice}$  is the average sea ice skin temperature and  $(T_{sk})_{water}$  is the open water counterpart. The ice edge is defined as the northernmost latitude where sea ice concentration is 10%.

During the winter expedition, a sharp drop of air temperature was observed while sailing into the MIZ (along a southward route; Fig. 1b), which corresponded to a smooth drop of skin temperature (Fig. 3a). Conversely, an increase of temperature was reported on the way out. The outermost samples, located within 100 km from the edge, were taken in partially ice covered waters, with concentrations in the range 40-90%. From the image inspection and observations onboard, the sea ice comprised new ice formation such as grease, frazil and, more sporadically, pancakes. The skin temperature varied from a maximum of  $-2^{\circ}\text{C}$  to a minimum of  $-4^{\circ}\text{C}$ ; air temperature was  $\approx -5^{\circ}\text{C}$ . Despite the narrow range, the pdf displays two close, and yet evident, peaks on either side of the freezing temperature, separating sea ice from open water fractions (Fig. 3b). The samples in the band 100-200 km from the ice edge were dominated by pancakes (thickness of 0.3-0.8 m). The sea ice fraction increased to 90-100% and the skin temperature was  $-10^{\circ}\text{C} < T_{sk} < -5^{\circ}\text{C}$ . A notable vertical gradient was reported with air temperature being approximately  $5^{\circ}\text{C}$  colder than the skin temperature. At 110 km, the pdf showed a well developed bimodality (Fig. 3c). The ice-type population around the freezing temperature was equivocal as it mixed water and grease/frazil ice. However, the peak emerging at  $\approx -5^{\circ}\text{C}$  represented pancake ice distinctly. Whereas the separation between the two peaks was net, there was a large number of data points between the peaks. These rep-

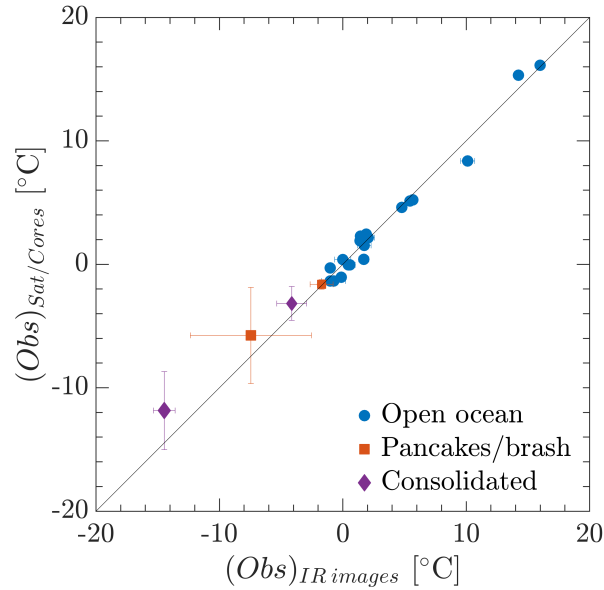


**Figure 2.** Thermal imaging against satellite data and core measurements. For open ocean conditions, observations of the sea surface skin temperature from the IR camera are compared against skin temperature from satellite sensors. In the MIZ (pancake/brash and consolidated ice), the sea ice skin temperature from the IR camera are compared against sea ice near-surface temperature (i.e. 2.5 cm below the surface) from ice cores. The error bars represent the observation ranges.

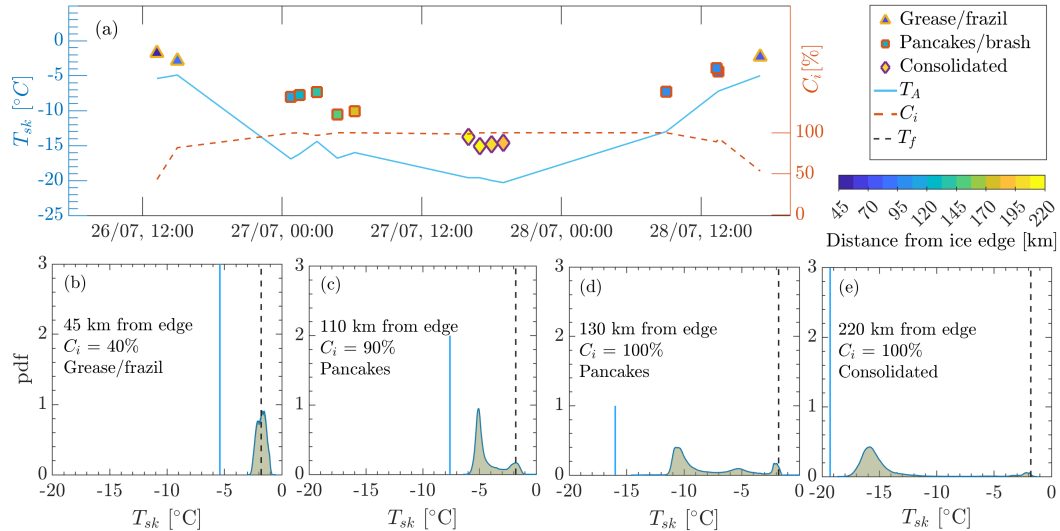


**Figure 3.** Skin temperature in the marginal ice zone during the winter expedition (Fig. 1b): (a) bulk weighted average as a function of time (x-axis) and distance from the edge (color code); (b-e) examples of probability density functions of skin temperature at various distances from the ice edge. As reference, air temperature ( $T_A$ ), freezing temperature ( $T_f$ ) and sea ice concentration ( $C_i$ ) are reported.

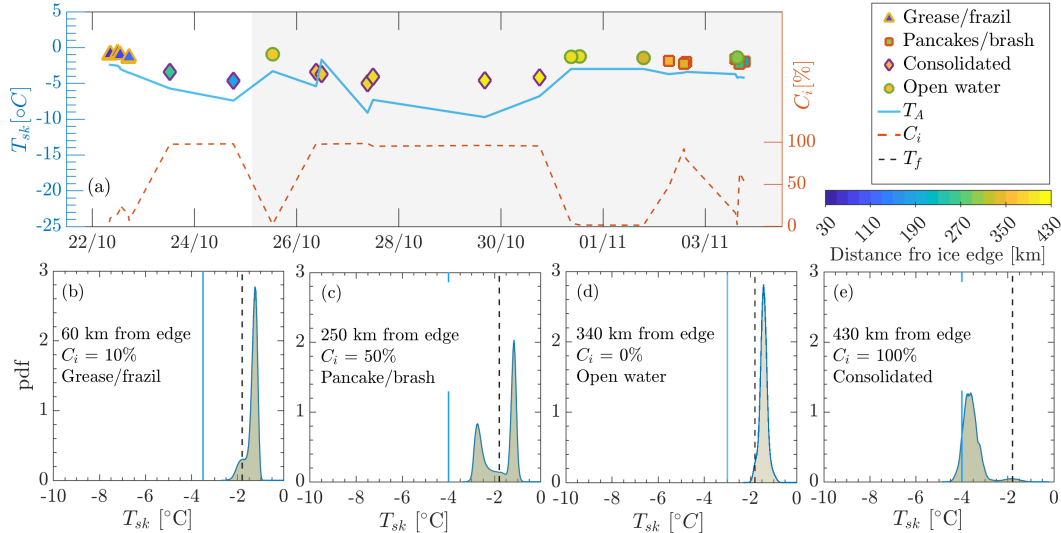


**Figure 4.** As in 3 but for the spring expedition (Fig. 1c). Data within the grey shaded area in (a) refer to observations taken along the eastward route (longitudes 0-24°E; cf. Fig. 1c).

309 represent a mixture of grease and frazil ice, which formed in the interstitial space (see Figs.  
 310 1d,e). Further South in the pancake region (Fig. 3d), the skin temperature of sea ice cooled  
 311 down, denoting more mature pancake floes. A neat separation between ice types confers  
 312 the pdf a characteristic trimodal form: the peak at  $-10.5^{\circ}\text{C}$  represent pancakes; the  
 313 peak at  $-5.5^{\circ}\text{C}$  is grease/frazil ice; and the peak around freezing temperature is a mix  
 314 of open water and grease/frazil ice. Over  $\approx 200$  km from the edge, the sea ice cover was  
 315  $\approx 100\%$ , with thickness of  $\approx 1$  m, which originated from pancake welding. Leads of vari-  
 316 able lengths and width were common in the region (Figs. 1f,g). The thermal vertical gra-  
 317 dient remained approximately  $5^{\circ}\text{C}$ . The pdf resumes a bimodal feature in consolidated  
 318 sea ice at 220 km from the edge (Fig. 3e). Sea ice skin temperature is centred at  $-16^{\circ}\text{C}$ ,  
 319 while warmer water emerging from leads gives rise to a lesser peak at  $\approx -2.5^{\circ}\text{C}$ . It is  
 320 worth noting that no sea ice of any form was observed in the openings. Hence, the cold  
 321 temperature in the leads is attributed to super-cooled water (cf. Haumann et al., 2020).

322 In spring (Fig. 4), the MIZ exhibited a more variable composition. Throughout the  
 323 spring expedition, the air temperature was consistently colder than the skin tempera-  
 324 ture, with a vertical gradient of  $\approx 2 - 3^{\circ}\text{C}$ . The image sample from the outermost region  
 325 was characterised by scattered formation of grease ice with  $C_i < 30\%$ . This region  
 326 extended for  $\approx 150$  km from the edge (about half way through the southward route; see  
 327 Fig. 1c). The significant weight of open water fractions in this band resulted in a stable  
 328 skin temperature with distance from the edge, which was consistently above freezing.  
 329 The pdf is markedly narrower than in winter (Fig. 4b) with a dominant open water  
 330 mode at  $\approx -1.36^{\circ}\text{C}$ . A smaller second peak centred at about the freezing tempera-  
 331 ture is also visible. The identification of the ice type from this secondary peak is am-  
 332 biguous as it is in between the skin temperature of water and the grease/frazil ice tem-  
 333 perature found in winter. The sample taken from the region between 150 and 300 km  
 334 from the edge (second half of the southward route) was consistently dominated by com-  
 335 pacted ice with leads ( $C_i \approx 100\%$ ). Although a large open water fraction was reported  
 336 at the beginning of the eastward route (cf. Fig. 1c), compact ice remained the prevail-  
 337 ing ice type along the first half of the eastward transect (0-12° E; data within 26/10 and  
 338 30/10 in Fig. 4a), noting the vessel also sailed further South until about 450 km from  
 339 the edge. The averaged skin temperature was  $\approx -5^{\circ}\text{C}$ . The pdf is dominated by the  
 340 sea ice partition with a secondary peak just above the freezing temperature denoting open

341 water from leads (Fig. 4e). Further East (longitudes 12-24°E; Fig. 1c), the average skin  
 342 temperature increased to  $\approx -2^\circ\text{C}$ . This section of the transect followed a northeasterly  
 343 route, moving from about 450 to 250 km from the ice edge. Sea ice conditions changed  
 344 into a disarranged mixture of new pancake formations, pancake-like floes from broken-  
 345 up consolidated ice, and occasional large leads and open water fractions of size up to ap-  
 346 proximately 10 km, as visually detected from the images and the onboard observations  
 347 (Hepworth et al., 2020). In this cluster of images, the sea ice concentration was highly  
 348 variable between 0-100% (see data within 01/11 and 03/11 in Fig. 4a). The pdf shows  
 349 evident bimodality in region dominated by pancake-like floes (Fig. 4c) and a distinctive  
 350 unimodality centered at temperature above freezing in regions of open water (Fig. 4d).

### 351 4.3 Heat fluxes

352 The heat fluxes computed from eqs. 1-8 for all the acquired image clusters are sum-  
 353 marised in Fig. 5. The absorbed shortwave radiation is small over winter as the upper  
 354 interquartile range does not exceed  $5 \text{ Wm}^{-2}$ . Sporadic records acquired at solar noon  
 355 reached values up to  $\approx 50 \text{ Wm}^{-2}$ . In spring, the shortwave radiation increased, but so  
 356 did the spread with the interquartile range  $\approx 15 - 150 \text{ Wm}^{-2}$ , noting that the lowest  
 357 values are associated to nighttime or periods of extended cloud coverage and the largest  
 358 coincide with observations at solar noon. The net longwave radiation exhibited a sim-  
 359 ilarly narrow spread in both seasons. Energy losses varied between  $-60$  and  $-30 \text{ Wm}^{-2}$   
 360 in winter and  $-40$  and  $-10 \text{ Wm}^{-2}$  in spring.

361 Also the latent flux remained small in winter and with a narrow spread from  $-50$   
 362 to  $-10 \text{ Wm}^{-2}$ . It instead increased in spring and showed a larger variability spanning  
 363 from  $-100$  to  $0 \text{ Wm}^{-2}$ , primarily due to the higher changes in humidity (cf. Fig. B1).

364 The sensible flux was the most substantial energy loss in winter with magnitude  
 365 spanning from  $-150$  to  $-30 \text{ Wm}^{-2}$  due to large thermal gradient between the ocean and  
 366 the atmosphere. Conversely, it was less intense and both positive and negative in spring  
 367  $-30 \text{ Wm}^{-2}$  and  $20 \text{ Wm}^{-2}$  owing to the smaller gradient (Fig. 4a).

368 The total energy flux in winter was negative, mostly due to the low shortwave ra-  
 369 diation flux and the large negative latent heat flux. This is expected during the sea ice  
 370 advance period. In spring, the median was also negative; the spread was large spanning  
 371 from  $-120$  to  $250 \text{ Wm}^{-2}$  but skewed towards the negative values. This indicates a pos-  
 372 sible sea ice growth phase that coexisted with the onset of breakup during spring, par-  
 373 ticularly explaining the observations of both new pancake formations and brash ice from  
 374 broken-up compact ice found in the eastern part of the track.

## 375 5 Comparison with ERA5 reanalyses

### 376 5.1 Reanalysis products and matching with field observations

377 There are several publicly available climate reanalysis products. Here we adopt the  
 378 ERA5 data set from the European Centre for Medium-Range Weather Forecasts (ECMWF;  
 379 Hersbach et al., 2020), which produces hourly variables with a spatial resolution of  $0.25^\circ$ .  
 380 An intercomparison of air-sea variables and energy fluxes from different reanalysis prod-  
 381 ucts in the Southern Ocean is discussed in Liu et al. (2011) and Yu et al. (2019). As-  
 382 sessment against in-situ measurements in the Antarctic MIZ shows that the ECMWF's  
 383 reanalysis is the most accurate (Yu et al., 2019), motivating the decision to use the ERA5  
 384 as benchmark.

385 For consistency with field observations (§3), basic atmospheric variables were re-  
 386 trieved from ERA5 and applied as input in eqs. (1-8) to estimate radiation and turbu-  
 387 lent fluxes. Variables were recovered at ship's locations with compatible reanalysis out-  
 388 put times, through linear interpolations between nearby grid points. To build compa-

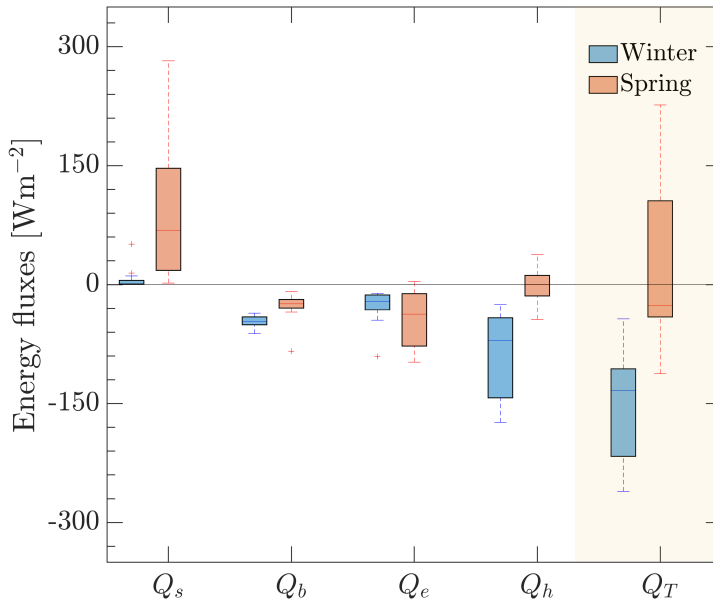


**Figure 5.** Box-and-whisker plots of the energy flux components ( $Q_s$ ,  $Q_b$ ,  $Q_e$  and  $Q_h$ ) and the total budget ( $Q_T$ ). The boxes represent the interquartile range (25<sup>th</sup>-75<sup>th</sup> percentiles); the central mark of the box indicates the median; whiskers extend to the most extreme data points not considered outliers; + symbols are outliers.

389 rable and collocated field observations, in-situ data falling in the ERA5’s grid box of side  
 390  $0.25^\circ$  containing the ship’s position and within a time window of  $\pm 30$  minutes relative  
 391 to the reanalysis were selected and averaged.

392 In the following, we present the comparison of skin temperature, sea ice concen-  
 393 tration, and the resulting fluxes computed from these and other ancillary variables from  
 394 observations and ERA5. The other atmospheric variables are shown in Appendix B. A  
 395 further comparison between the estimated fluxes and those obtained directly from ERA5  
 396 is presented in Appendix A for completeness.

## 397 5.2 Sea ice concentration

398 The sea ice fraction in the reanalysis was  $\approx 35\%$  lower than observed in the IR  
 399 data (Fig. 6a). This discrepancy is evident for all the ice types seen in the images over  
 400 a spatial range of more than 200 km, which comprises about 10 pixels of the original satel-  
 401 lite data prescribed in ERA5. Interestingly, the assimilated ice fraction was always  $C_i \leq$   
 402  $80\%$ . Discrepancies are the largest in pancake ice images, where the concentration pro-  
 403 vided by ERA5 is two-thirds of the observed one. In this region, the satellite algorithm  
 404 only identified mature and larger pancake floes, but it did not capture the interstitial  
 405 grease/frazil ice that was detected as ice free. This is in contrast with the conditions re-  
 406 ported by Alberello et al. (2019) during winter in the Indian Ocean sector, in which in-  
 407 terstitial sea ice between pancake floes was instead identified as ice, resulting in 100%,  
 408 apparently consolidated ice cover despite the observed substantial wave propagation (Alberello  
 409 et al., 2022). It is therefore complex to distinguish the winter mixture of pancakes and  
 410 interstitial ice from space, and satellites return contrasting concentration values from sim-  
 411 ilar surfaces.

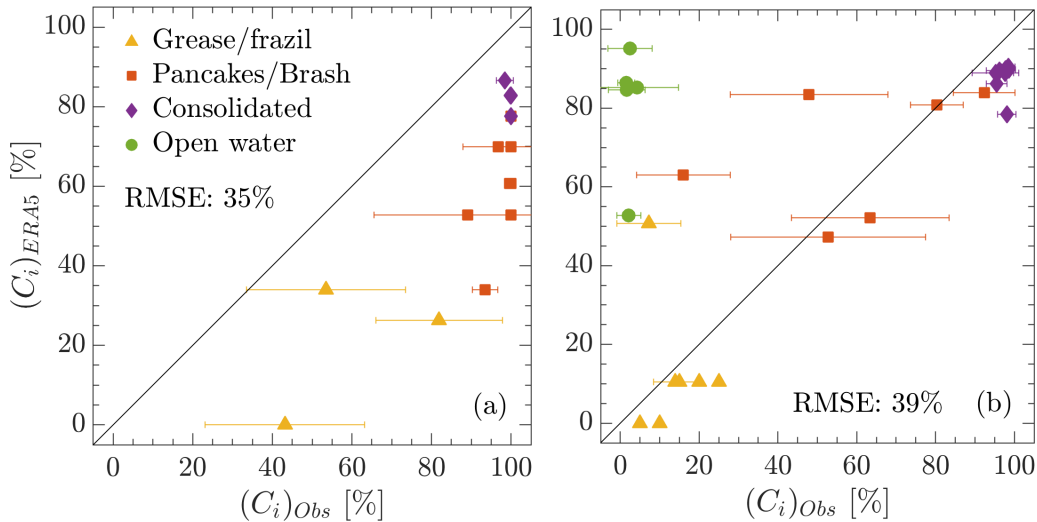


**Figure 6.** Sea ice concentration from ERA5 versus in-situ observations from IR images for the winter (upper panels) and spring (lower panels) expeditions: (a) winter; and (b) spring. The threshold for partitioning the sea ice fraction in the IR images was the freezing temperature ( $T_{fr} = -1.865^{\circ} \text{C}$ ). Error bars represents the observation range.

412 The comparison improves in spring (Fig. 6b). The images containing grease/frazil  
 413 and consolidated ice (southward transect and first half of the eastward transect—longitude  
 414  $0\text{-}12^{\circ}\text{E}$ ; Fig. 1) were better represented in the ice cover fraction prescribed in ERA5, al-  
 415 though there was still a tendency to underestimate the concentration. Data from lon-  
 416 gitudes  $12\text{-}24^{\circ}\text{E}$  along the eastward transect (Fig. 1) showed evident inconsistencies be-  
 417 tween the reanalysis and in-situ observations. While several data points were captured  
 418 by ERA5, some others were overpredicted by 30-40%. This region was also complicated  
 419 by the presence of large openings. These were not detected by the reanalysis, which pre-  
 420 dicted almost full sea ice coverage instead of 0-5% reported in-situ. The presence of open  
 421 water patches was the main reason for the large root mean squared error (RMSE) of  $\approx$   
 422 40%.

### 423 5.3 Skin temperature

424 In ERA5, the ocean surface is partitioned into sea ice and open water. The skin  
 425 temperature in sea ice is estimated from the layer one sea ice surface temperature (ISTL1;  
 426 i.e. the temperature at 3.5 cm depth in bare ice) through the conductivity coefficient,  
 427 while its open water counterpart is a function of the bulk sea surface temperature (SST,  
 428 (See details in ECMWF, 2016b)). The overall skin temperature is computed as a weighted  
 429 average following eq. 9. Since the skin temperature for individual partitions is not avail-  
 430 able for download, we used ISTL1 and SST in our analysis when considering ice and open  
 431 water separately.

432 The comparison with in-situ data is presented in Fig. 7 for winter and spring. Pan-  
 433 els (a,c) distinguish the ocean and ice partitions. The in-situ skin temperature of sea ice  
 434 is compared against ISTL1, which is the only near-surface product available in ERA5,  
 435 while skin temperature of open ocean is compared against the ERA5 SST. We acknowl-

436 edge the different depths between in-situ data and ERA5, although it is expected that  
 437 the thermal gradient between the skin and an immediate sub-layer is confined within  $1^\circ\text{C}$   
 438 and the sub-layers are warmer than the surface (Talley, 2011; ECMWF, 2016b). In win-  
 439 ter, the SST compared well with observations, indicating that differences between skin  
 440 and sub-layer temperature are indeed minimal. Deviations emerged in the MIZ, depend-  
 441 ing on the sea ice type. Differences were negligible in grease/frazil ice, while they increased  
 442 by several degrees in pancake conditions and slightly reduced again in consolidated ice.  
 443 The overall RMSE in the MIZ was about  $4^\circ\text{C}$ , with a mean bias of  $-3.5^\circ\text{C}$  (i.e. ISTL1  
 444 is colder than observations). This discrepancy is significant because ISTL1 is expected  
 445 to be equal or warmer than the actual skin temperature of sea ice. The relevance of the  
 446 error is further confirmed by the core measurements taken at 2.5 cm from the surface,  
 447 and thus more comparable with ISTL1, which were indeed warmer than the skin tem-  
 448 perature of sea ice from the IR images (Fig. 2) and thus also warmer than ISTL1. In spring,  
 449 in-situ and ERA5 data were more similar, although ISTL1 remained slightly colder than  
 450 the observed skin temperature (RMSE  $\approx 1.74^\circ\text{C}$  and mean bias  $\approx -1.4^\circ\text{C}$ ) and an ev-  
 451 ident deviation emerged for consolidated sea ice conditions.

452 The weighted skin temperature computed with eq. 9 in winter improves with re-  
 453 spect to the sea ice partition (Fig. 7b), except for a few pancake ice images. The RMSE  
 454 reduces to  $\approx 1.0^\circ\text{C}$ . Recalling that the skin temperature mediates sea ice and open wa-  
 455 ter fractions, this improvement is attributed to an artificial effect arising from uncertain-  
 456 ties in the sea ice concentration and ISTL1. Excessively cold ISTL1 in ERA5 are coun-  
 457 terbalanced by a large fractions of open water, contributing to warming the skin dispro-  
 458 proportionately. Hence, it is the compensation of errors that justifies the accurate match  
 459 of skin temperature in Fig. 7b.

460 In spring, the skin temperature compared relatively well with field data. The er-  
 461 ror compensation reported in winter is not evident as the more homogeneous temper-  
 462 ature distribution attenuates the differences in sea ice concentration (Fig. 6b, with the  
 463 notable exception of the missing open water leads). The RMSE remains similar between  
 464 the partitioned and the weighted skin temperatures, with a mean bias of  $\approx -0.9^\circ\text{C}$ .

#### 465 5.4 Radiative, turbulent and total heat fluxes

466 The radiative, turbulent and total heat fluxes are reported in Figs. 8 and 9 for the  
 467 winter and spring expeditions, respectively. In winter, the solar radiation ( $Q_s$ ) from ERA5  
 468 is mostly consistent with observations apart from an evident overestimation by  $40\text{-}100\text{ Wm}^{-2}$   
 469 in regions dominated by grease/frazil and pancake ice, where discrepancies in sea ice con-  
 470 centration exceed 50% (Fig. 6a). The net longwave radiation and turbulent fluxes from  
 471 the reanalysis show a systematic overestimation: the RMSE is  $\approx 9.8\text{ Wm}^{-2}$  for  $Q_b$ ,  $\approx$   
 472  $15.8\text{ Wm}^{-2}$  for  $Q_e$  and  $\approx 32.5\text{ Wm}^{-2}$  for  $Q_h$ . Differences are particularly significant for  
 473 turbulent fluxes as they always exceed the observation range. The ERA5 total flux (neg-  
 474 ative as dominated by losses) is, to some extent, consistent with the observations. There  
 475 is an evident overestimation, but this is generally within the relatively large observation  
 476 range (Fig. 8e). The RMSE of  $\approx 62.5\text{ Wm}^{-2}$  is attributed to the underestimation of skin  
 477 temperature. This is confirmed in Fig. 8f, in which the total energy flux from ERA5 is  
 478 recomputed using the in-situ skin temperature. This correction reduces the RMSE by  
 479 about 50%. The substitution of the other atmospheric variables shown in Appendix B  
 480 produces lesser effects on the total budget than the skin temperature.

481 In spring (Fig. 9), the main difference is found in  $Q_s$ , with the reanalysis overes-  
 482 timating the solar radiation flux by  $50\text{-}200\text{ Wm}^{-2}$ . Given that the sea ice concentration  
 483 is mostly well-captured (Fig. 6b, with the exception of some open-water conditions as  
 484 discussed below), this error cannot be attributed to the ice cover imposed to ERA5. The  
 485 disagreement comes directly from the downward solar radiation flux that differs by the  
 486 same magnitude when compared to the ship sensor (see Fig. B1). The solar radiation

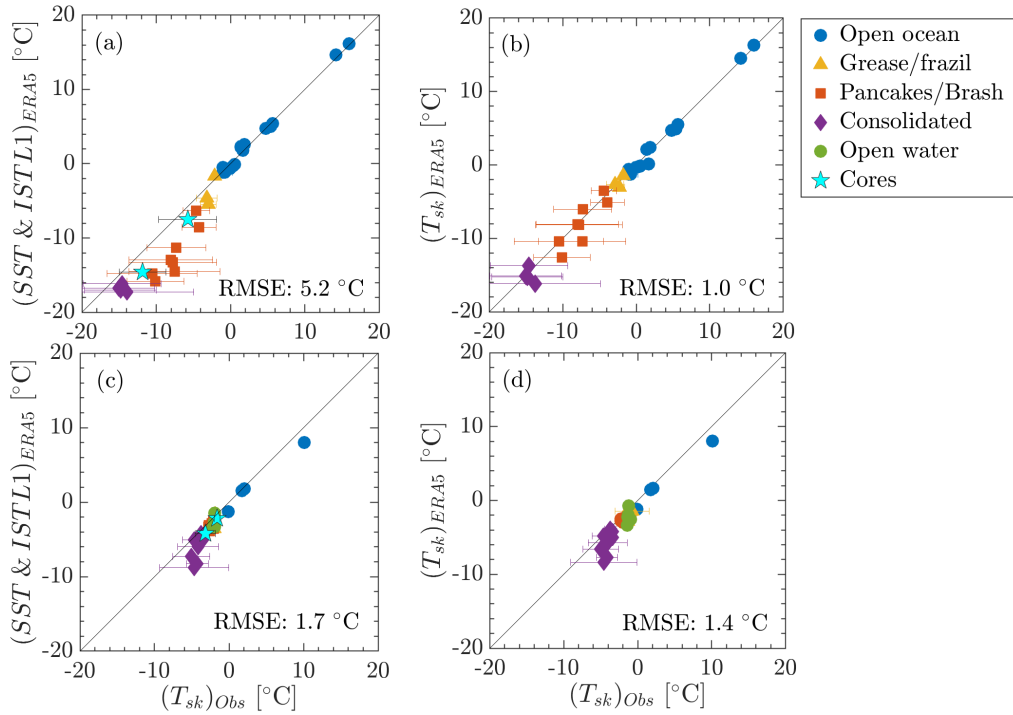


**Figure 7.** Comparison of surface temperature for the winter (upper panels) and spring (lower panels) expeditions: (a,c) sea ice surface temperature (ISTL1, at 2.5 cm below the surface) in the MIZ and bulk sea surface temperature for open ocean from ERA5 are compared against the sea ice partition of the skin temperature in the MIZ and water skin temperature in the open ocean from IR images; and (b,d) the weighted average overall skin temperature from ERA5 is compared against the IR images counterpart. Error bars represents observation range. The RMSE refer to the portion of data points in the MIZ.

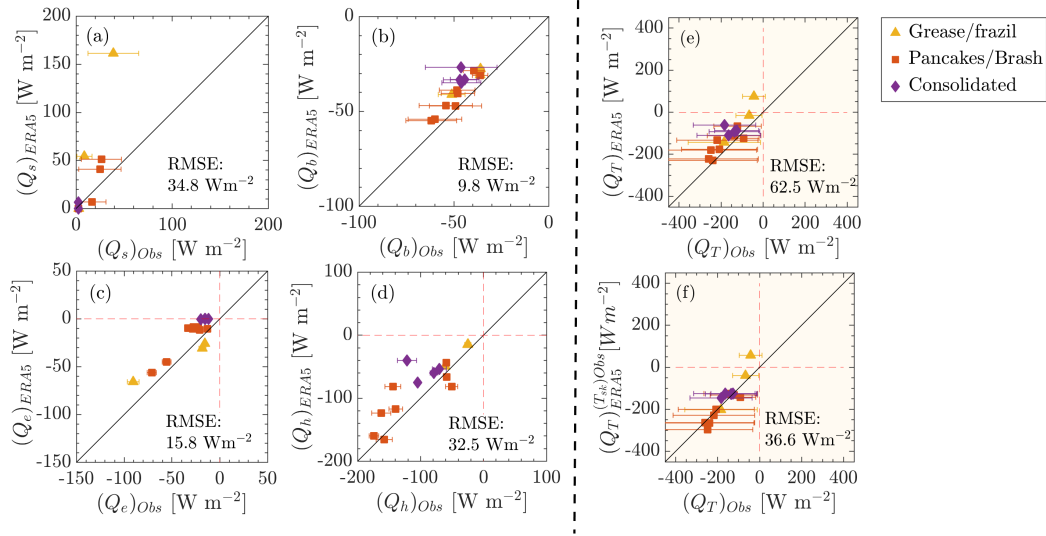


**Figure 8.** Energy flux components computed using air-sea variables from ERA5 versus estimations based on in-situ observations for the winter (a-d). Total energy flux computed using atmospheric variables from ERA5 (e) and ERA5 forced by in-situ skin temperature (f) versus estimations based on in-situ observations for the winter. Error bars represent observation range.

487 in summer is known to be affected by inaccuracies in the cloud coverage simulations (e.g.  
 488 Flato et al., 2014; Yu et al., 2019; Fiddes et al., 2022) and this is confirmed also in spring  
 489 in this region. Interestingly, there is a small subset of data for which  $Q_s$  is underestimated  
 490 by the reanalysis by  $\approx 100 \text{ Wm}^{-2}$ . This is instead due to the use of the wrong sea ice  
 491 surface, because it corresponds to the low-albedo of open water fractions (longitudes 12-  
 492  $24^\circ\text{E}$  of the eastward transect), which are seen as consolidated ice by ERA5. The long-  
 493 wave radiation ( $Q_b$ ) and the sensible ( $Q_h$ ) flux were captured reasonably well with RMSE  
 494  $\approx 7$  and  $34 \text{ Wm}^{-2}$ , respectively. The scatter is attributed to discrepancies in the skin  
 495 temperature. The latent heat flux shows a larger spread with an evident underestima-  
 496 tion of observations in the sector of mature sea ice conditions and overestimation in grease/frazil  
 497 ice, with an overall RMSE of  $\approx 45 \text{ Wm}^{-2}$ . These errors are attributed to inaccuracies  
 498 in simulating wind speed and the saturated and specific humidities as shown in Fig. B1.  
 499 Unlike winter, the total budget is dominated by  $Q_s$  and most of the locations show an  
 500 evident energy gain in the reanalysis. Relative to in-situ data, ERA5 has a negative bias  
 501 with fluxes consistently overestimated (Fig. 9e), noting that there are examples, across  
 502 all ice types, where reanalysis exhibits gain while loss was reported in the field. A few  
 503 samples in pancake and open water regions are underestimated. These differences depend  
 504 on errors in atmospheric variables such as skin temperature, wind speed and hu-  
 505 midity (cf. Appendix B). However, the largest impact in spring is due to the inadequate  
 506 representation of  $Q_s$  in ERA5. The recalculated total energy flux in which the in-situ  
 507  $Q_s$  replaces the ERA5 values is more in agreement with the measurements and reduces  
 508 the RMSE by approximately 60% (Fig. 9f). Similarly to the winter case, the other sub-  
 509 stitutions do not produce a similar improvement.

## 510 6 Conclusions

511 High-resolution infrared images of the uppermost layer of the ocean surface were  
 512 acquired during winter and spring expeditions to the Antarctic marginal ice zone in the  
 513 Eastern Weddell sea sector. Images provided data on the skin temperature and morphol-  
 514 ogy of the heterogeneous surface, which were eventually converted into sea ice concen-

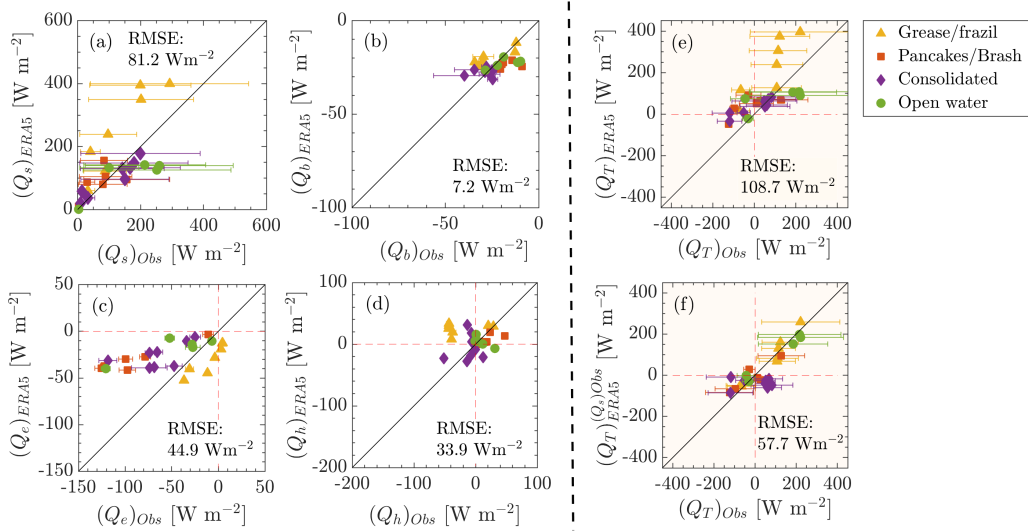


**Figure 9.** As in Fig. 8 but for the spring expedition; panel (f) shows ERA5 forced by the in-situ intake of solar radiation ( $Q_S$ ) versus estimations based on in-situ observations.

515 tration. Combined with other atmospheric variables measured onboard, these were applied to estimate radiative and turbulent heat fluxes over the ice-free and ice-covered ocean  
 516 portions through bulk formulae and compared with output variables from the ERA5 re-  
 517 analysis.  
 518

519 In winter, the sea ice cover was an organised compound of several, neatly separated  
 520 in space, sea ice types. The external region within  $\approx 100$  km of the ice edge was domi-  
 521 nated by young ice formations, including grease, frazil and newly formed pancakes. This  
 522 was followed by a region of more mature pancakes between  $\approx 100 - 200$  km from the  
 523 edge, with interstitial spaces occupied by either water or grease/frazil ice. Consolidated  
 524 sea ice with leads was observed beyond 200 km from the ice margin. IR images revealed  
 525 sharp inhomogeneities of the skin temperature in the exterior MIZ due to the coexistence  
 526 of several sea ice type and open water fractions, and a more uniform distribution in con-  
 527 solidated ice. The total energy balance was dominated by losses through the net long-  
 528 wave radiation and turbulent latent and sensible heat fluxes, with the latter being the  
 529 main contributor by one order of magnitude. Despite a notable variability, which was  
 530 also reported in one of the few earlier studies on the topic (Lytle et al., 2000), the losses  
 531 were in the order of  $-10^2$   $\text{W m}^{-2}$ , underpinning the winter sea ice growth.

532 The ERA5 matches observations of skin temperature reasonably well, despite a ten-  
 533 dency to predict a colder surface (a similar small bias was reported in Cerovečki et al.,  
 534 2022). We found that this apparent agreement is forced by compensation of errors. On  
 535 one side, the sea ice partition is far colder than observations, while on the other the re-  
 536 analysis exhibits a smaller sea ice fraction. Open waters result in a significant warming  
 537 of the skin temperature, hence counterbalancing the colder sea ice skin. Due to this com-  
 538 pensation, energy fluxes from ERA5 are ultimately compatible with observations, although  
 539 biased towards less intense fluxes. These result in a more moderate energy loss than in-  
 540 situ, which we attribute to the small, yet relevant, uncertainties in skin temperature. To  
 541 a certain extent, this is also reported in King et al. (2022); Cerovečki et al. (2022), which  
 542 link it to biases of the downward component of the longwave radiation.

543 The spring data showed a more homogeneous distribution of skin temperature with  
 544 less sharp thermal contrast between water and sea ice partitions. Yet, this reflected a

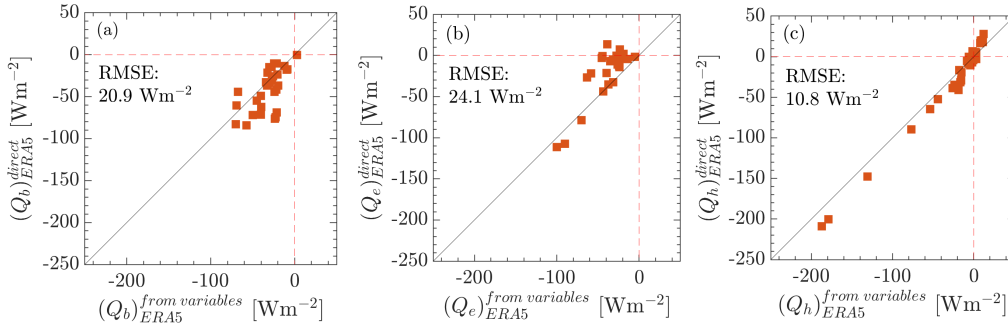


**Figure A1.** Example of net longwave radiation flux (a), latent heat flux (b) and sensible heat flux (c) estimated from the bulk formulae in eqs. (1-8) with ERA5 air-sea variables as input against those provided directly by ERA5. Data are from a single grid point located along the ship’s route at about 150 km from the ice edge and for every day at 12pm of the month of July (2019).

545 disarrayed sea ice cover, comprising large open water fractions as far as 400 km from the  
 546 ice edge, young ice formations and more mature sea ice conditions originating from both  
 547 growth and breakup. Sea ice concentration was erratic and ranged 0-100%, even deep  
 548 in the sea ice region. Despite an intense intake of solar radiation relative to winter, the  
 549 total energy fluxes showed a large spread spanning from losses to gains with the distri-  
 550 bution skewed towards the former. This substantiates a particularly complex sea ice dy-  
 551 namics in spring, where melt and growth are concurrent.

552 Reanalysis represents skin temperature well over spring, despite a persistent small  
 553 cold bias. The error compensation that is reported in winter is not evident. The total  
 554 energy flux from reanalysis shows a more complicated relationship with observations than  
 555 in winter. Reanalysis produces a consistent energy gain during the observation period  
 556 and does not capture the alternation of gains and losses reported in-situ. Our results in-  
 557 dicate that the biases in shortwave radiation estimates from ERA5 reported by other au-  
 558 thors in summer are the dominant source of error also in spring.

559 Observations presented herein contribute a step further in our understanding of com-  
 560 plex air-sea interaction processes in the Antarctic marginal ice zone, especially in the still  
 561 largely unexplored winter season. It is essential that such high resolution measurements  
 562 become routine on voyages to Antarctica across all seasons. This would contribute to  
 563 a more comprehensive sampling of sea ice in several geographical sectors, providing vi-  
 564 tal data for unravelling the dynamics driving the sea ice cycle and improving both mod-  
 565 els and remote sensing products.

## 566 Appendix A Vertical invariant scaling and roughness length approach

567 The ERA5 computes the fluxes using near-surface temperature (SST and ISTL1),  
 568 other atmospheric variables and transfer coefficients for turbulent fluxes based on char-  
 569 acteristic length scales (ECMWF, 2016a). In the main text, the fluxes from ERA5 were  
 570 computed with the bulk formulae in eqs. (1-8) using the skin temperature and other at-  
 571 mospheric variables from ERA5 as input and transfer coefficients for turbulent fluxes based  
 572 on a vertical invariant scaling. A comparison between these approaches is presented in  
 573 Fig. A1 for the winter net longwave radiation, latent, and sensible heat fluxes.

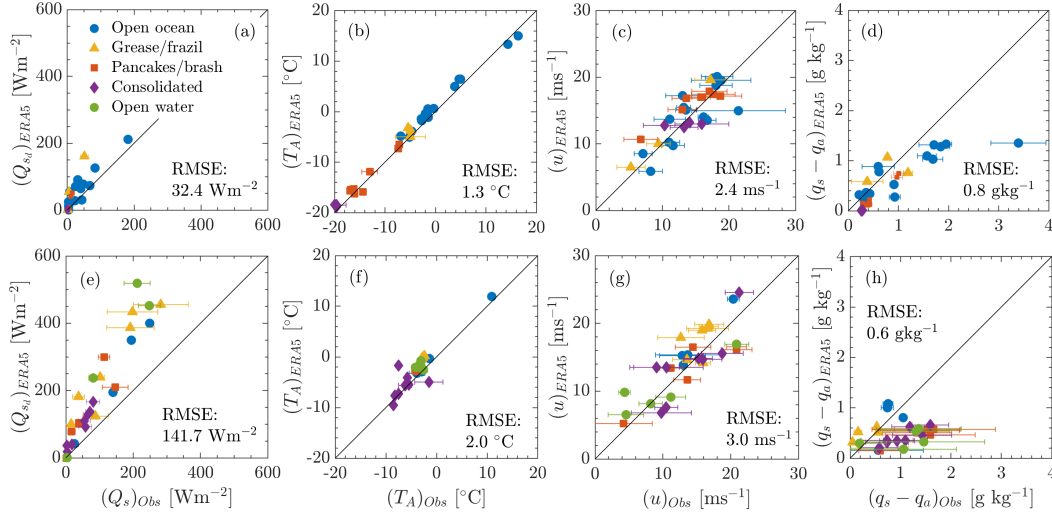


**Figure B1.** Comparison between in-situ observations from the meteorological station aboard the S.A. Agulhas II and reanalysis from ERA5 for the winter (a-d) and spring (e-h) expeditions: (a-e) downward solar radiation; (b-f) air temperature; (c-g) 10-metre wind speed; and (d-g) the difference between saturated and specific humidity.

## Appendix B Other atmospheric variables and comparison with reanalysis

The comparison between in-situ and ERA5 data for other relevant air-sea variables (i.e. downward solar radiation, air temperature, wind speed, and the difference between saturated and specific humidity) is reported in Fig. B1. Note that some basic atmospheric variables such as air temperature and pressure have been assimilated in the ERA5 and, hence, these supporting data are not totally independent from reanalysis. In winter, ERA5 is, to a certain extent, consistent with in-situ observations. However, there is an evident tendency to over estimate downward radiation ( $\text{RMSE} \approx 32 \text{ Wm}^{-2}$ ) and wind speed ( $\text{RMSE} \approx 4 \text{ ms}^{-1}$ ). In spring, the downward solar radiation and wind speed are over estimated by the reanalysis with  $\text{RMSE} \approx 112 \text{ Wm}^{-2}$  and  $3 \text{ ms}^{-1}$ , respectively. The difference between saturated and specific humidity is under estimated in winter and spring ( $\text{RMSE} \approx 0.31 \text{ g kg}^{-1}$ ). The air temperature is well captured.

### Availability statement

Processed data from IR images (skin temperature and sea ice concentration) and supporting atmospheric variables that were used for this study are published in Zenodo and can be access through the link <https://doi.org/10.5281/zenodo.7943559>. ERA5 reanalysis can be downloaded from the Copernicus Climate Change Service (<https://cds.climate.copernicus.eu/#!/home>). The codes used to process thermal imaging and perform the analysis are available upon request to the corresponding authors.

### Authors contribution

Conceptualization: IT, AA, MV, MO, AT; Methodology: IT, MV, AT; Investigation: IT, AA, GM, MV, AT; Visualization: IT; Supervision: AT, AA, MV; Writing—original draft: IT, AA, GM, MV, MO, AT; Writing—review & editing: IT, AA, GM, MV, MO, AT.

## Acknowledgments

The expeditions were funded by the South African National Antarctic Programme through the National Research Foundation. AA and AT were funded by the ACE Foundation and Ferring Pharmaceuticals and the Australian Antarctic Science Program (project 4434). AA acknowledges support from the Japanese Society for the Promotion of Science (PE19055) and the London Mathematical Society (Scheme 5 – 52206). AT acknowledges support from the Australia Research Council (DP200102828). MV was supported by the NRF SANAP contract UID118745. GM acknowledges support from the Swedish Foundation for International Cooperation in Research and Higher Education (project no. SA2017-7063). IT and AT thank Dr J. Bidlot (ECMWF) and Dr L. Aouf (Meteo France) for support with the ERA5 products. We are indebted to Captain Knowledge Bengu and the crew of the SA Agulhas II for their invaluable contribution to data collection We acknowledge Dr L. Fascette for technical support.

## References

- Alberello, A., Bennetts, L., Heil, P., Eayrs, C., Vichi, M., MacHutchon, K., ... Toffoli, A. (2020). Drift of pancake ice floes in the winter antarctic marginal ice zone during polar cyclones. *Journal of Geophysical Research: Oceans*, *125*(3), e2019JC015418.
- Alberello, A., Bennetts, L. G., Onorato, M., Vichi, M., MacHutchon, K., Eayrs, C., ... others (2022). Three-dimensional imaging of waves and floes in the marginal ice zone during a cyclone. *Nature communications*, *13*(1), 1–11.
- Alberello, A., Onorato, M., Frascoli, F., & Toffoli, A. (2019). Observation of turbulence and intermittency in wave-induced oscillatory flows. *Wave Motion*, *84*, 81–89.
- Andreas, E. L., Horst, T. W., Grachev, A. A., Persson, P. O. G., Fairall, C. W., Guest, P. S., & Jordan, R. E. (2010). Parametrizing turbulent exchange over summer sea ice and the marginal ice zone. *Quarterly Journal of the Royal Meteorological Society*, *136*(649), 927–943.
- Audh, R. R., Johnson, S., Hambrock, M., Marquart, R., Pead, J., Rampai, T., ... Vichi, M. (2022, August). *Sea ice core temperature and salinity data collected during the 2019 SCALE Spring Cruise*. Zenodo. Retrieved from <https://doi.org/10.5281/zenodo.6997631> (This research has been funded by the National Research Foundation of South Africa (NRF)) doi: 10.5281/zenodo.6997631
- Bechtold, P. (2009). Atmospheric thermodynamics. *ECMWF Lecture Notes*, *22*.
- Bharti, V., Fairall, C. W., Blomquist, B. W., Huang, Y., Protat, A., Sullivan, P. P., ... Manton, M. J. (2019). Air-sea heat and momentum fluxes in the southern ocean. *Journal of Geophysical Research: Atmospheres*, *124*(23), 12426–12443.
- Biri, S., Cornes, R. C., Berry, D. I., Kent, E. C., & Yelland, M. J. (2023). Airseafluxcode: Open-source software for calculating turbulent air-sea fluxes from meteorological parameters. *Frontiers in Marine Science*, *9*. doi: 10.3389/fmars.2022.1049168
- Bourassa, M. A., Gille, S. T., Bitz, C., Carlson, D., Cerovecki, I., Clayson, C. A., ... Wick, G. A. (2013). High-latitude ocean and sea ice surface fluxes: Challenges for climate research. *Bulletin of the American Meteorological Society*, *94*(3), 403–423.
- Brandt, R. E., Warren, S. G., Worby, A. P., & Grenfell, T. C. (2005). Surface albedo of the antarctic sea ice zone. *Journal of Climate*, *18*(17), 3606–3622.
- Brouwer, J., Fraser, A. D., Murphy, D. J., Wongpan, P., Alberello, A., Kohout, A., ... Williams, G. D. (2022). Altimetric observation of wave attenuation through the antarctic marginal ice zone using icesat-2. *The Cryosphere*, *16*(6), 2325–2353. Retrieved from <https://tc.copernicus.org/articles/16/2325/2022/> doi: 10.5194/tc-16-2325-2022

- 652 Buck, A. L. (1981). New equations for computing vapor pressure and enhancement  
653 factor. *Journal of Applied Meteorology and Climatology*, *20*(12), 1527–1532.
- 654 Cerovečki, I., Sun, R., Bromwich, D. H., Zou, X., Mazloff, M. R., & Wang, S.-H.  
655 (2022). Impact of downward longwave radiative deficits on antarctic sea-ice  
656 extent predictability during the sea ice growth period. *Environmental Research  
657 Letters*, *17*(8), 084008.
- 658 Chin, T. M., Vazquez-Cuervo, J., & Armstrong, E. M. (2017). A multi-scale high-  
659 resolution analysis of global sea surface temperature. *Remote sensing of envi-  
660 ronment*, *200*, 154–169.
- 661 Dieckmann, G. S., & Hellmer, H. H. (2010). The importance of sea ice: an overview.  
662 *Sea ice*, *2*, 1–22.
- 663 Dong, S., Sprintall, J., Gille, S. T., & Talley, L. (2008). Southern ocean mixed-  
664 layer depth from argo float profiles. *Journal of Geophysical Research: Oceans*,  
665 *113*(C6).
- 666 ECMWF. (2016a). *IFS Documentation Cy41r2 Part IV: Physical Processes* (Tech.  
667 Rep.). European Centre for Medium-Range Weather Forecasts. Retrieved from  
668 <https://www.ecmwf.int/en/publications/ifs-documentation>
- 669 ECMWF. (2016b). *IFS Documentation Cy43r1 Part V: Ensemble Predic-  
670 tion System* (Tech. Rep.). European Centre for Medium-Range Weather  
671 Forecasts. Retrieved from [https://www.ecmwf.int/en/publications/  
672 ifs-documentation](https://www.ecmwf.int/en/publications/ifs-documentation)
- 673 Fan, P., Pang, X., Zhao, X., Shokr, M., Lei, R., Qu, M., ... Ding, M. (2020). Sea ice  
674 surface temperature retrieval from landsat 8/tirs: Evaluation of five methods  
675 against in situ temperature records and modis ist in arctic region. *Remote  
676 Sensing of Environment*, *248*, 111975.
- 677 Fiddes, S. L., Protat, A., Mallet, M. D., Alexander, S. P., & Woodhouse, M. T.  
678 (2022). Southern ocean cloud and shortwave radiation biases in a nudged  
679 climate model simulation: does the model ever get it right? *Atmospheric  
680 Chemistry and Physics Discussions*, 1–34.
- 681 Flato, G., Marotzke, J., Abiodun, B., Braconnot, P., Chou, S. C., Collins, W., ...  
682 Rummukainen, M. (2014). Evaluation of climate models. In *Climate change  
683 2013: the physical science basis. contribution of working group i to the fifth  
684 assessment report of the intergovernmental panel on climate change* (pp. 741–  
685 866). Cambridge University Press.
- 686 Gryschka, M., Drüe, C., Etling, D., & Raasch, S. (2008). On the influence of sea-  
687 ice inhomogeneities onto roll convection in cold-air outbreaks. *Geophysical Re-  
688 search Letters*, *35*(23).
- 689 Hall, D. K., Nghiem, S. V., Rigor, I. G., & Miller, J. A. (2015). Uncertainties of  
690 temperature measurements on snow-covered land and sea ice from in situ and  
691 modis data during bromex. *Journal of Applied Meteorology and Climatology*,  
692 *54*(5), 966–978.
- 693 Haumann, F. A., Moorman, R., Riser, S. C., Smedsrud, L. H., Maksym, T., Wong,  
694 A. P. S., ... Sarmiento, J. L. (2020). Supercooled southern ocean waters.  
695 *Geophysical Research Letters*, *47*(20), e2020GL090242.
- 696 Hepworth, E., Vichi, M., Engelbrecht, M., Kaplan, K., Sandru, A., Bossau, J., ...  
697 Rogerson, J. J. (2020). *Sea Ice Observations in the Antarctic Marginal Ice  
698 Zone during Spring 2019* [data set]. PANGAEA. Retrieved from [https://  
699 doi.org/10.1594/PANGAEA.921755](https://doi.org/10.1594/PANGAEA.921755) doi: 10.1594/PANGAEA.921755
- 700 Hersbach, H., Bell, B., Berrisford, P., Hirahara, S., Horányi, A., Muñoz-Sabater, J.,  
701 ... others (2020). The era5 global reanalysis. *Quarterly Journal of the Royal  
702 Meteorological Society*, *146*(730), 1999–2049.
- 703 Horvat, C. (2021). Marginal ice zone fraction benchmarks sea ice and climate model  
704 skill. *Nature communications*, *12*(1), 1–8.
- 705 Horvat, C., & Tziperman, E. (2018). Understanding melting due to ocean eddy heat  
706 fluxes at the edge of sea-ice floes. *Geophysical Research Letters*, *45*(18), 9721–

- 9730.
- 707 Huguenin, M. F., Holmes, R. M., & England, M. H. (2022). Drivers and distribu-  
708 tion of global ocean heat uptake over the last half century. *Nature Communi-*  
709 *cations*, *13*(1), 1–11.
- 710 Johnson, J. H., Flittner, G. A., & Cline, M. W. (1965). *Automatic data processing*  
711 *program for marine synoptic radio weather reports* (No. 503). US Department  
712 of the Interior, Bureau of Commercial Fisheries.
- 713 Johnson, S., Audh, R. R., de Jager, W., Matlakala, B., Vichi, M., Womack, A., &  
714 Rampai, T. (2023). Physical and morphological properties of first-year antarctic  
715 sea ice in the spring marginal ice zone of the atlantic-indian sector. *Journal*  
716 *of Glaciology*, 1–14. doi: 10.1017/jog.2023.21
- 717 King, J. C., Marshall, G. J., Colwell, S., Arndt, S., Allen-Sader, C., & Phillips,  
718 T. (2022). The performance of the era-interim and era5 atmospheric re-  
719 analyses over weddell sea pack ice. *Journal of Geophysical Research*, *127*(9),  
720 e2022JC018805.
- 721 Kottmeier, C., & Engelbart, D. (1992). Generation and atmospheric heat exchange  
722 of coastal polynyas in the Weddell Sea. *Boundary-layer meteorology*, *60*(3),  
723 207–234.
- 724 Krishfield, R. A., & Perovich, D. K. (2005). Spatial and temporal variability of  
725 oceanic heat flux to the arctic ice pack. *Journal of Geophysical Research:*  
726 *Oceans*, *110*(C7).
- 727 Kwok, R., Cunningham, G. F., & Hibler III, W. D. (2003). Sub-daily sea ice motion  
728 and deformation from radarsat observations. *Geophysical Research Letters*,  
729 *30*(23).
- 730 Landwehr, S., Volpi, M., Haumann, F. A., Robinson, C. M., Thurnherr, I., Ferracci,  
731 V., ... Schmale, J. (2021). Exploring the coupled ocean and atmosphere sys-  
732 tem with a data science approach applied to observations from the antarctic  
733 circumnavigation expedition. *Earth System Dynamics*, *12*(4), 1295–1369. Re-  
734 trieved from <https://esd.copernicus.org/articles/12/1295/2021/> doi:  
735 10.5194/esd-12-1295-2021
- 736 Li, N., Li, B., Lei, R., & Li, Q. (2020). Comparison of summer arctic sea ice surface  
737 temperatures from in situ and modis measurements. *Acta Oceanologica Sinica*,  
738 *39*(9), 18–24.
- 739 Liu, J., Xiao, T., & Chen, L. (2011). Intercomparisons of air–sea heat fluxes over the  
740 southern ocean. *Journal of climate*, *24*(4), 1198–1211.
- 741 Lytle, V., Massom, R., Bindoff, N., Worby, A., & Allison, I. (2000). Wintertime  
742 heat flux to the underside of east antarctic pack ice. *Journal of Geophysical*  
743 *Research: Oceans*, *105*(C12), 28759–28769.
- 744 Massom, R., & Comiso, J. C. (1994). The classification of arctic sea ice types and  
745 the determination of surface temperature using advanced very high resolution  
746 radiometer data. *Journal of Geophysical Research: Oceans*, *99*(C3), 5201–  
747 5218.
- 748 Massom, R. A., Lytle, V. I., Worby, A. P., & Allison, I. (1998). Winter snow cover  
749 variability on east antarctic sea ice. *Journal of Geophysical Research: Oceans*,  
750 *103*(C11), 24837–24855.
- 751 McCree, K. J. (1972). Test of current definitions of photosynthetically active radia-  
752 tion against leaf photosynthesis data. *Agricultural meteorology*, *10*, 443–453.
- 753 McPhee, M. G., Ackley, S. F., Guest, P., Huber, B. A., Martinson, D. G., Morison,  
754 J. H., ... Stanton, T. P. (1996). The antarctic zone flux experiment. *Bulletin*  
755 *of the American Meteorological Society*, *77*(6), 1221–1232.
- 756 Merchant, C. J., Embury, O., Bulgin, C. E., Block, T., Corlett, G. K., Fiedler, E.,  
757 ... others (2019). Satellite-based time-series of sea-surface temperature since  
758 1981 for climate applications. *Scientific data*, *6*(1), 1–18.
- 759 Millero, F. (1978). Freezing point of sea water. *eighth report of the Joint Panel of*  
760 *Oceanographic Tables and Standards, appendix, 6*, 29–31.
- 761

- 762 Monin, A. S., & Obukhov, A. M. (1954). Basic laws of turbulent mixing in the  
763 surface layer of the atmosphere. *Contrib. Geophys. Inst. Acad. Sci. USSR*,  
764 *151*(163), e187.
- 765 Omatuku Ngongo, E., Audh, R. R., Hall, B., Skatulla, S., MacHutchon, K., Rampai,  
766 T., & Vichi, M. (2022, August). *Sea ice core temperature and salinity data*  
767 *collected during the 2019 SCALE Winter Cruise*. Zenodo. Retrieved from  
768 <https://doi.org/10.5281/zenodo.6997449> (This research has been funded  
769 by the National Research Foundation of South Africa (NRF) Another version  
770 of this data set has been published in Skatulla, S., Audh, R.R., Cook, A., Hep-  
771 worth, E., Johnson, S., Lupascu, D.C., MacHutchon, K., Marquart, R., Mielke,  
772 T., Omatuku, E. and Paul, F., 2022. Physical and mechanical properties of  
773 winter first-year ice in the Antarctic marginal ice zone along the Good Hope  
774 Line. *The Cryosphere*, *16*(7), pp.2899-2925. - this data set was not quality con-  
775 trolled prior to publications. Future use of the data should refer to the dataset  
776 published here.) doi: 10.5281/zenodo.6997449
- 777 O’Carroll, A. G., Armstrong, E. M., Beggs, H. M., Bouali, M., Casey, K. S., Corlett,  
778 G. K., ... others (2019). Observational needs of sea surface temperature.  
779 *Frontiers in Marine Science*, *6*, 420.
- 780 Rasmussen, T. A., Høyer, J. L., Ghent, D., Bulgin, C. E., Dybkjær, G., Ribergaard,  
781 M. H., ... Madsen, K. S. (2018). Impact of assimilation of sea-ice surface  
782 temperatures on a coupled ocean and sea-ice model. *Journal of Geophysical*  
783 *Research: Oceans*, *123*(4), 2440–2460.
- 784 Ryan-Keogh, T., & Vichi, M. (2022, January). *Scale-win19 & scale-spr19 cruise re-*  
785 *port*. Zenodo. Retrieved from <https://doi.org/10.5281/zenodo.5906324>  
786 doi: 10.5281/zenodo.5906324
- 787 Schmale, J., Baccarini, A., Thurnherr, I., Henning, S., Efraim, A., Regayre, L., ...  
788 Carslaw, K. S. (2019). Overview of the antarctic circumnavigation expedi-  
789 tion: Study of preindustrial-like aerosols and their climate effects (ace-space).  
790 *Bulletin of the American Meteorological Society*, *100*(11), 2260-2283. doi:  
791 10.1175/BAMS-D-18-0187.1
- 792 Skatulla, S., Audh, R. R., Cook, A., Hepworth, E., Johnson, S., Lupascu, D. C., ...  
793 Vichi, M. (2022). Physical and mechanical properties of winter first-year ice  
794 in the antarctic marginal ice zone along the good hope line. *The Cryosphere*,  
795 *16*(7), 2899–2925. doi: 10.5194/tc-16-2899-2022
- 796 Smith, S. D. (1988). Coefficients for sea surface wind stress, heat flux, and wind pro-  
797 files as a function of wind speed and temperature. *Journal of Geophysical Re-*  
798 *search: Oceans*, *93*(C12), 15467–15472.
- 799 Talley, L. D. (2011). *Descriptive physical oceanography: an introduction*. Academic  
800 press.
- 801 Untersteiner, N. (1964). Calculations of temperature regime and heat budget of sea  
802 ice in the central arctic. *Journal of Geophysical Research*, *69*(22), 4755–4766.
- 803 Vichi, M. (2022). An indicator of sea ice variability for the antarctic marginal ice  
804 zone. *The Cryosphere*, *16*(10), 4087–4106.
- 805 Vichi, M., Eayrs, C., Alberello, A., Bekker, A., Bennetts, L., Holland, D., ... others  
806 (2019). Effects of an explosive polar cyclone crossing the antarctic marginal ice  
807 zone. *Geophysical Research Letters*, *46*(11), 5948–5958.
- 808 Womack, A., Vichi, M., Alberello, A., & Toffoli, A. (2022). Atmospheric drivers of  
809 a winter-to-spring lagrangian sea-ice drift in the eastern antarctic marginal ice  
810 zone. *Journal of Glaciology*, *68*(271), 999–1013. doi: 10.1017/jog.2022.14
- 811 Worby, A. P., & Comiso, J. C. (2004). Studies of the antarctic sea ice edge and  
812 ice extent from satellite and ship observations. *Remote sensing of environment*,  
813 *92*(1), 98–111.
- 814 Worby, A. P., Geiger, C. A., Paget, M. J., Van Woert, M. L., Ackley, S. F., & De-  
815 Liberty, T. L. (2008). Thickness distribution of antarctic sea ice. *Journal of*  
*Geophysical Research: Oceans*, *113*(C5).

- 817 Yu, L., Jin, X., & Schulz, E. W. (2019). Surface heat budget in the southern ocean  
818 from 42° s to the antarctic marginal ice zone: four atmospheric reanalyses  
819 versus icebreaker aurora australis measurements. *Polar Research*.
- 820 Yu, L., Jin, X., Schulz, E. W., & Josey, S. A. (2017). Air-sea interaction regimes in  
821 the sub-antarctic southern ocean and antarctic marginal ice zone revealed by  
822 icebreaker measurements. *Journal of Geophysical Research: Oceans*, *122*(8),  
823 6547–6564.
- 824 Zwally, H. J., Comiso, J. C., Parkinson, C. L., Cavalieri, D. J., & Gloersen, P.  
825 (2002). Variability of antarctic sea ice 1979–1998. *Journal of Geophysical*  
826 *Research: Oceans*, *107*(C5), 9–1.

Figure 1.

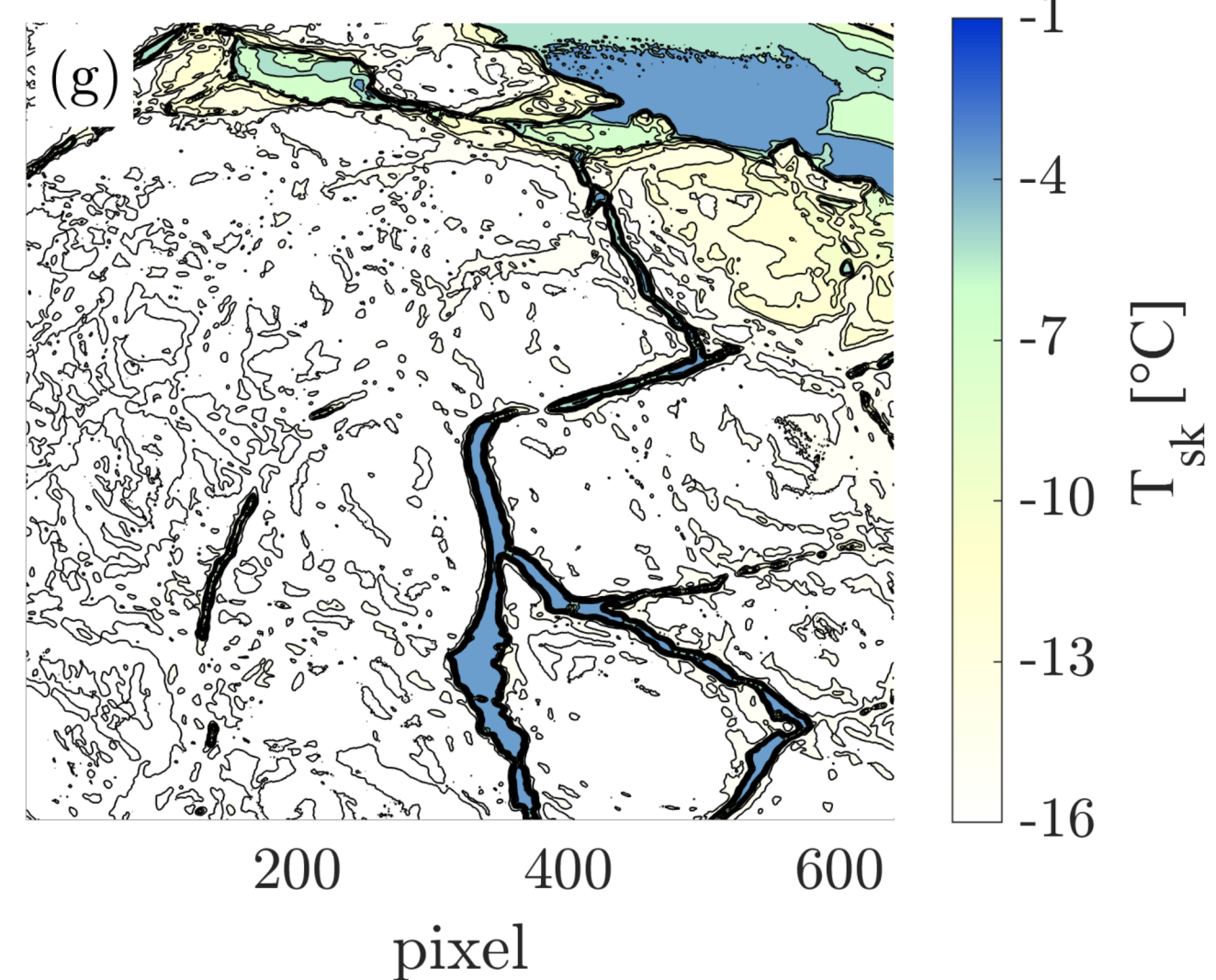
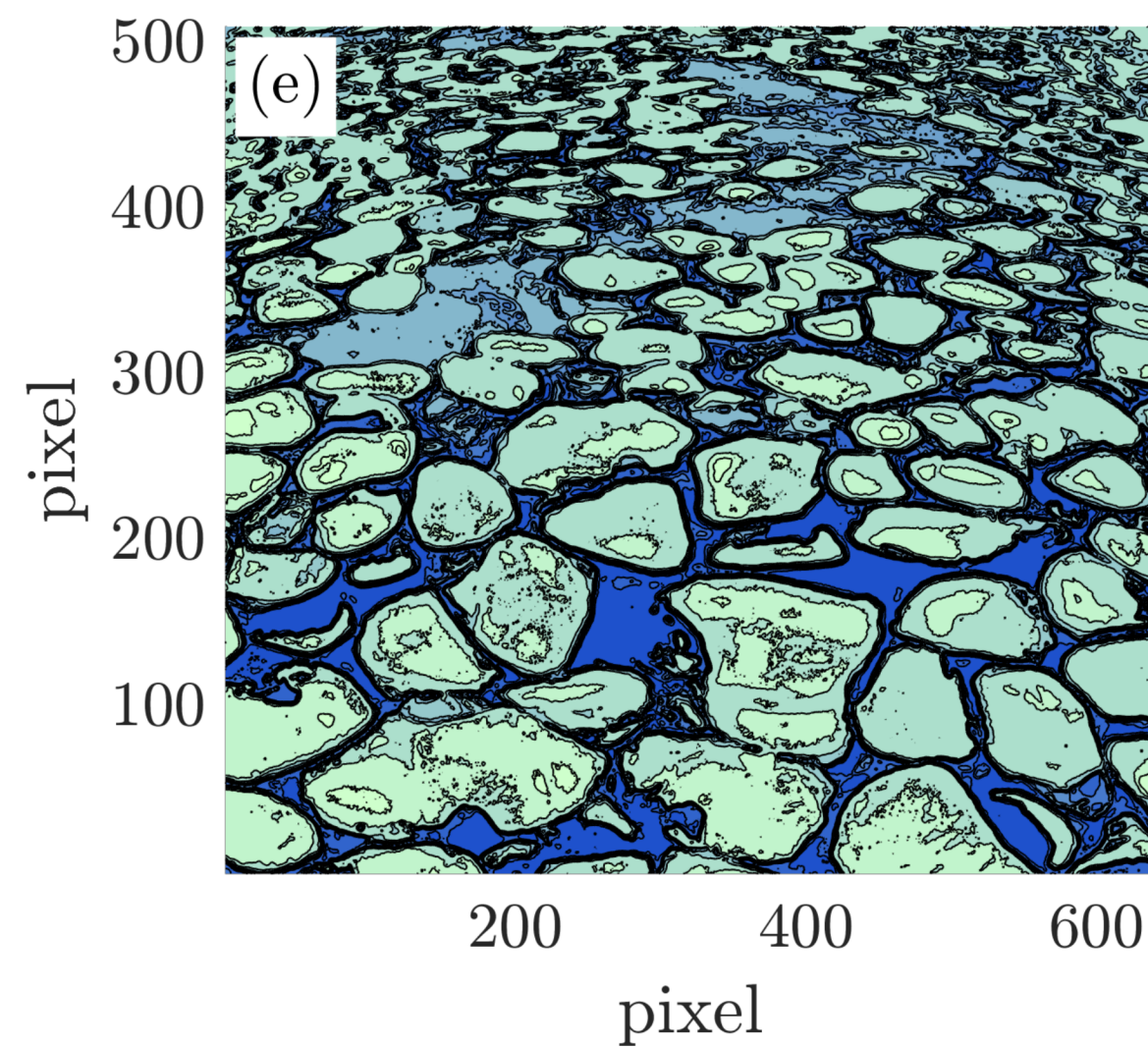
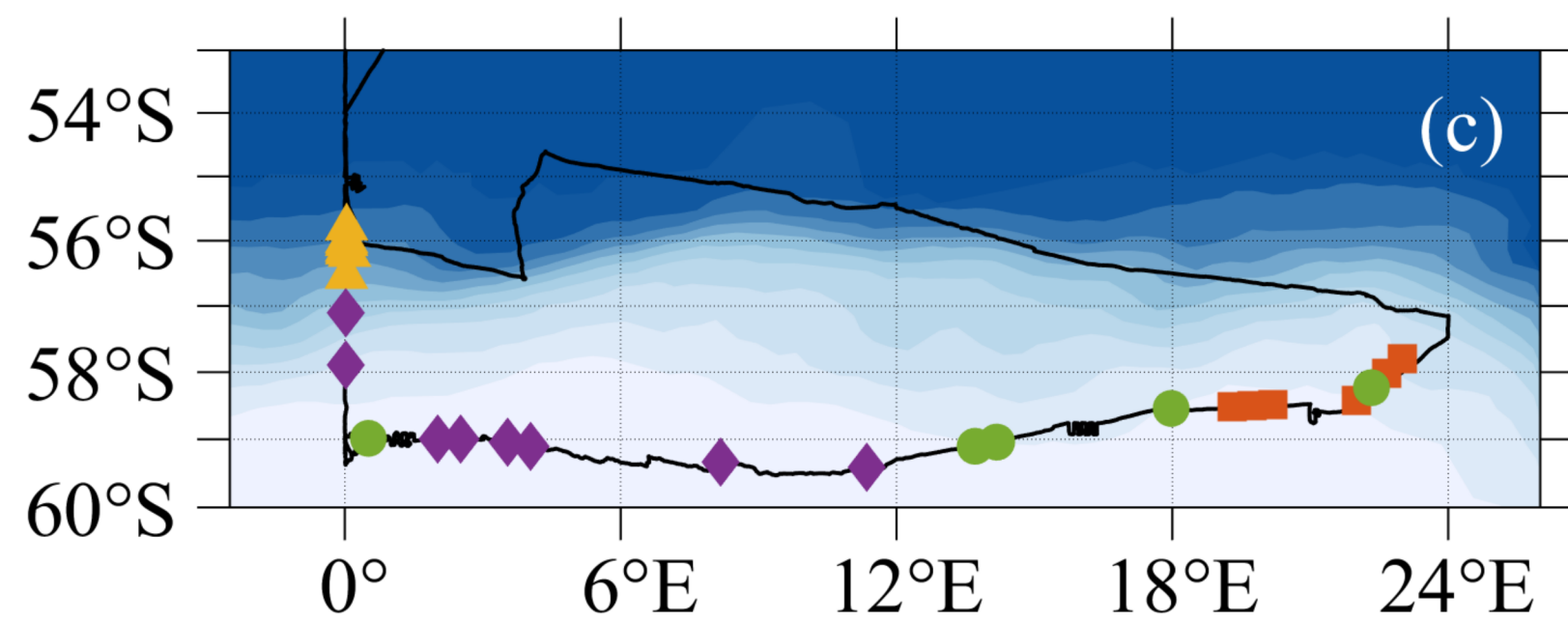
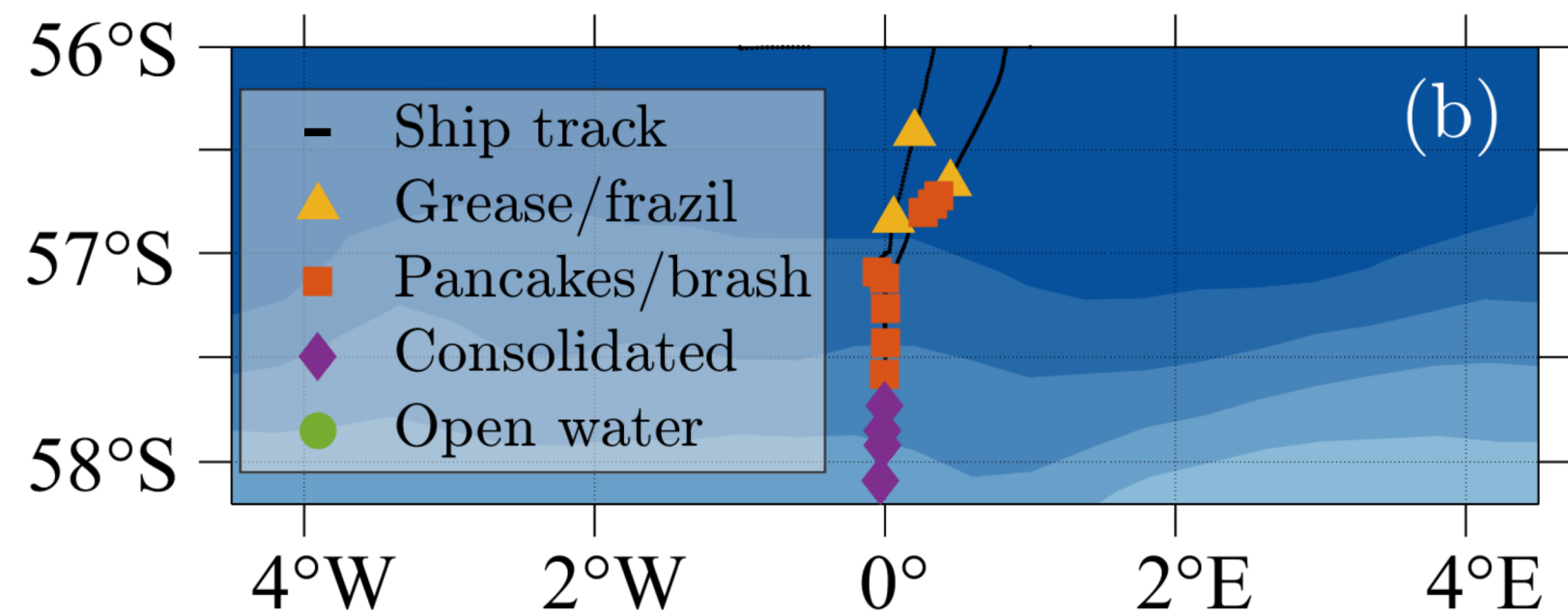
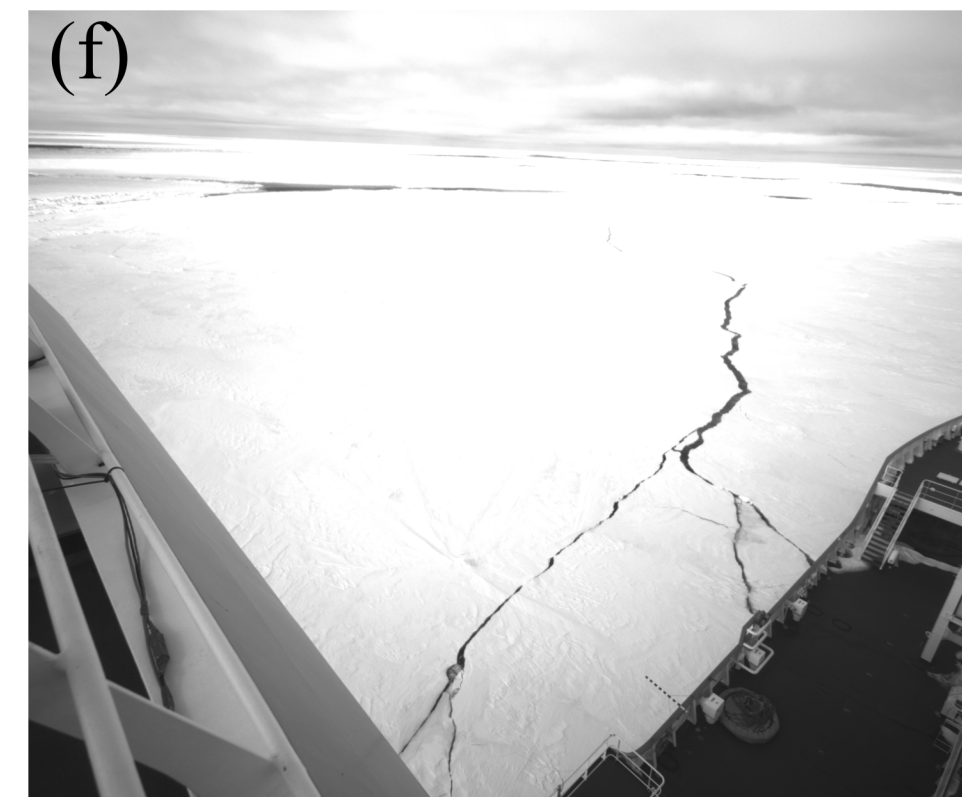
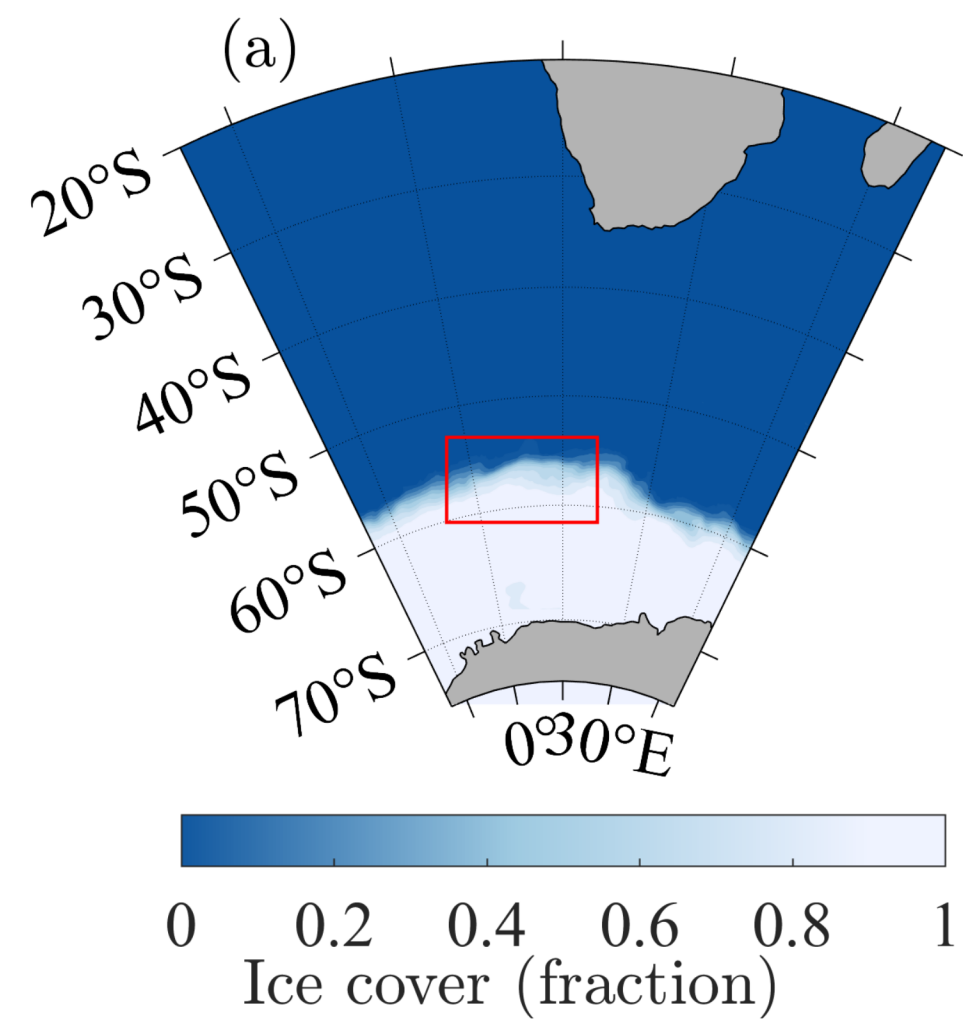


Figure 2.



Figure 3.

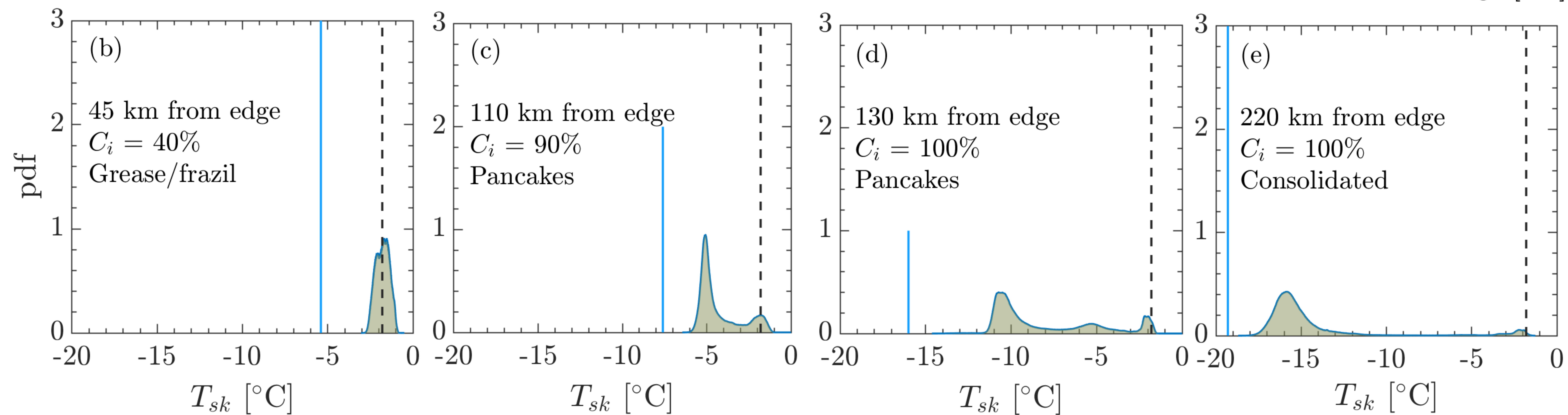
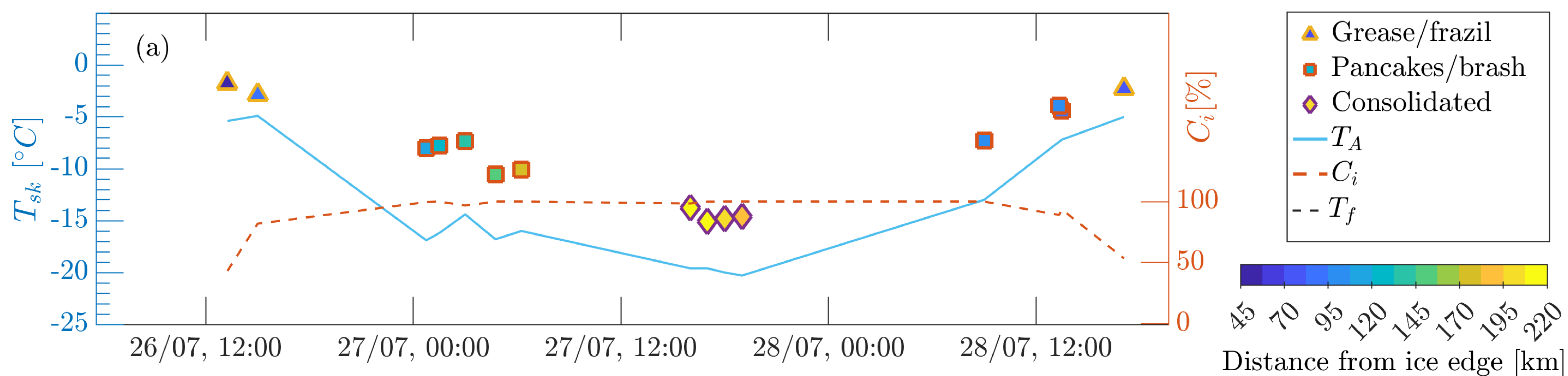


Figure 4.

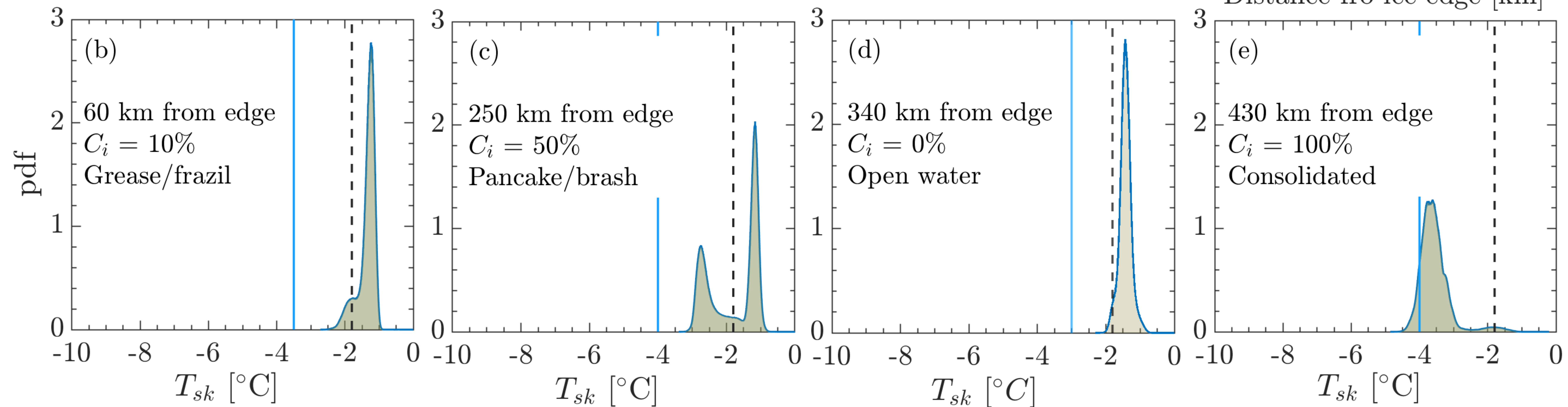
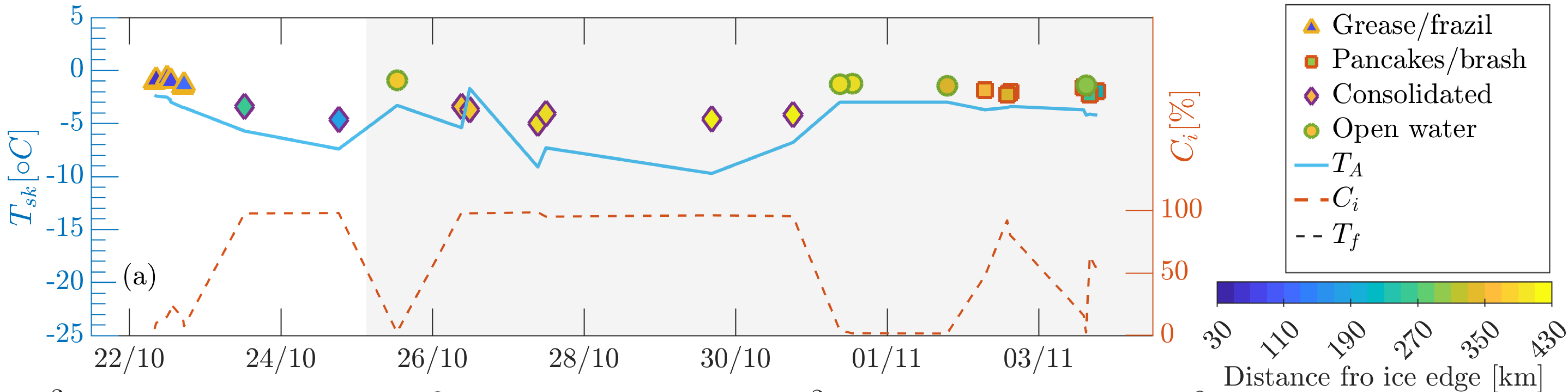


Figure 5.

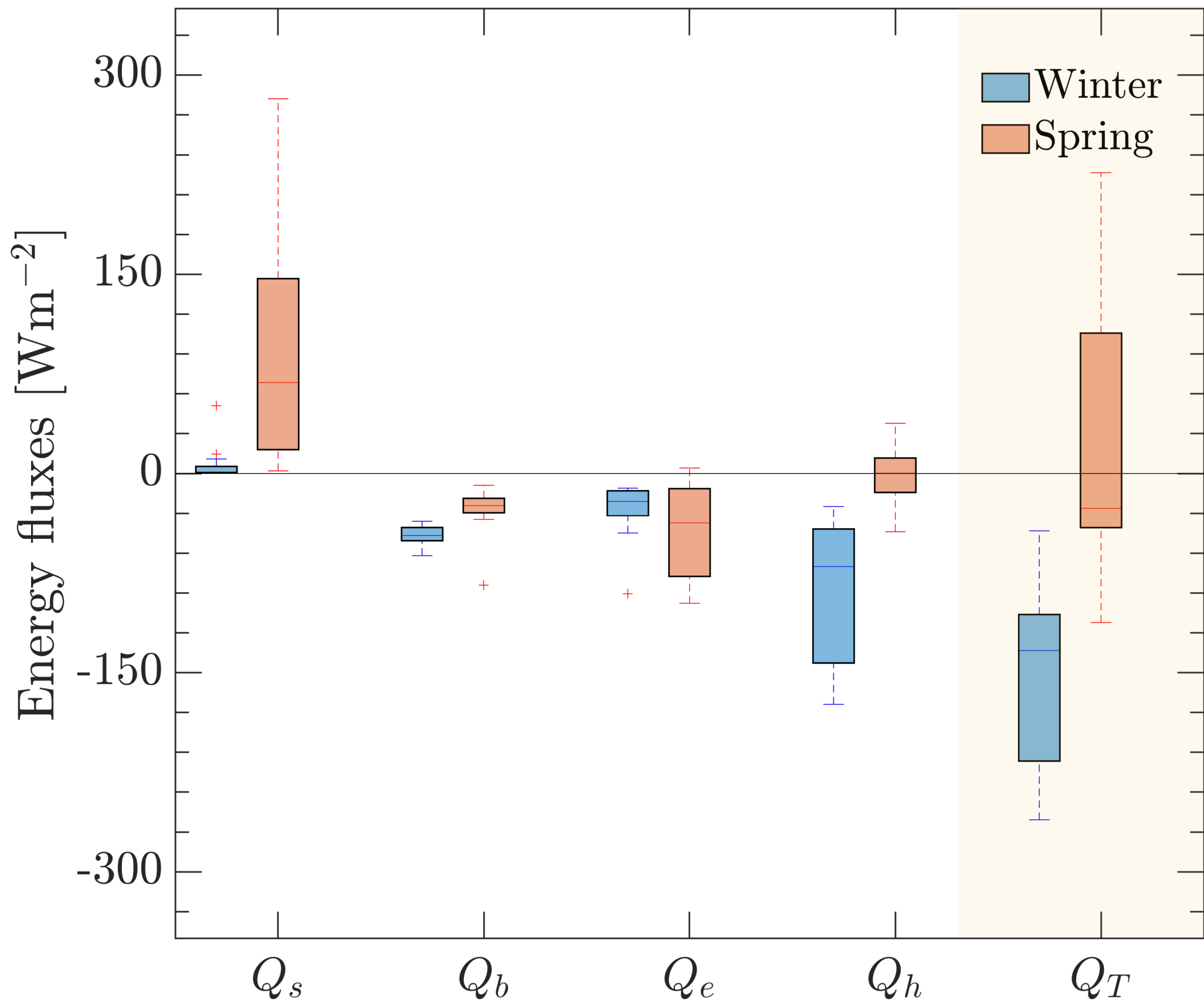


Figure 6.



Figure 7.

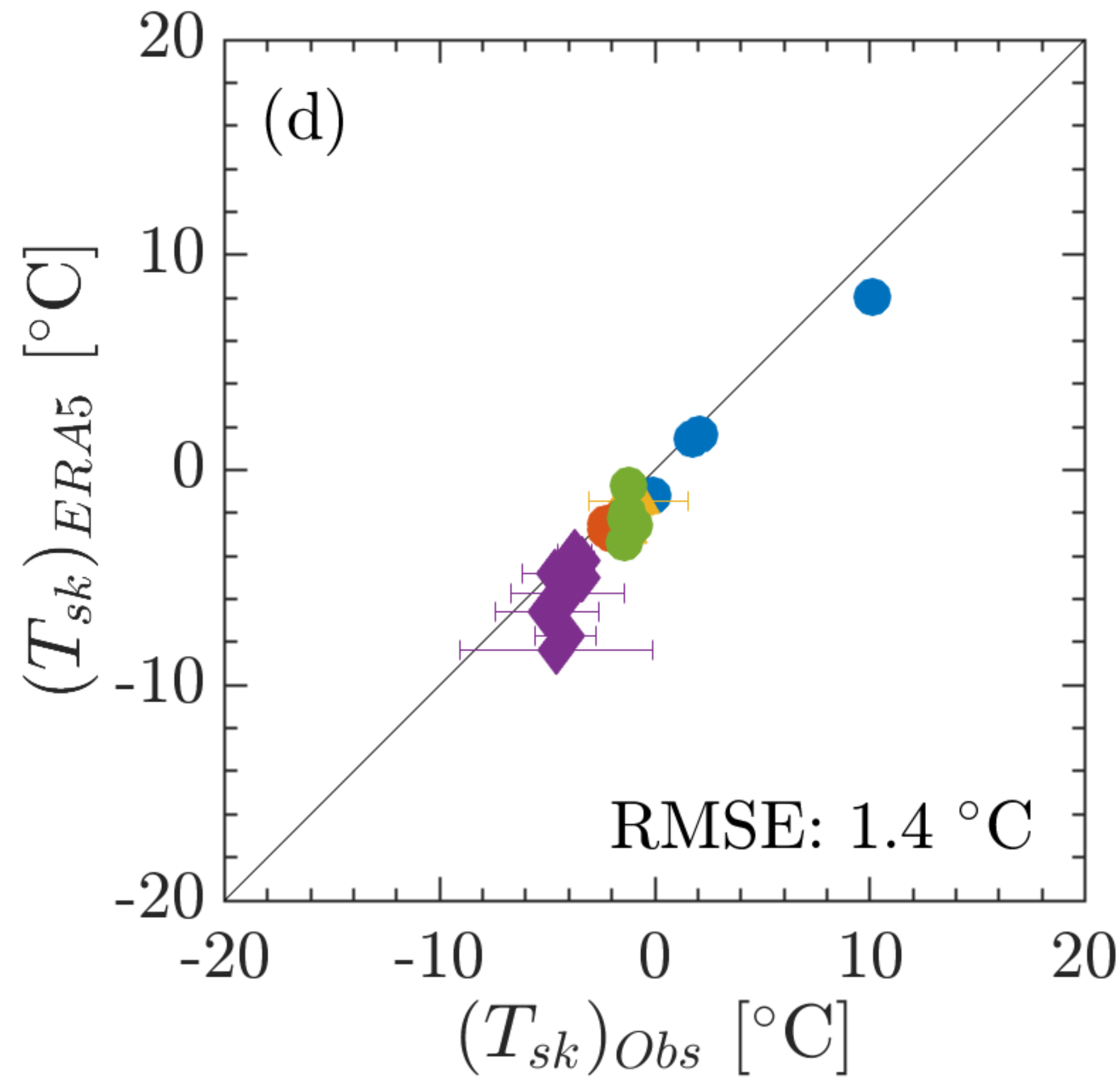
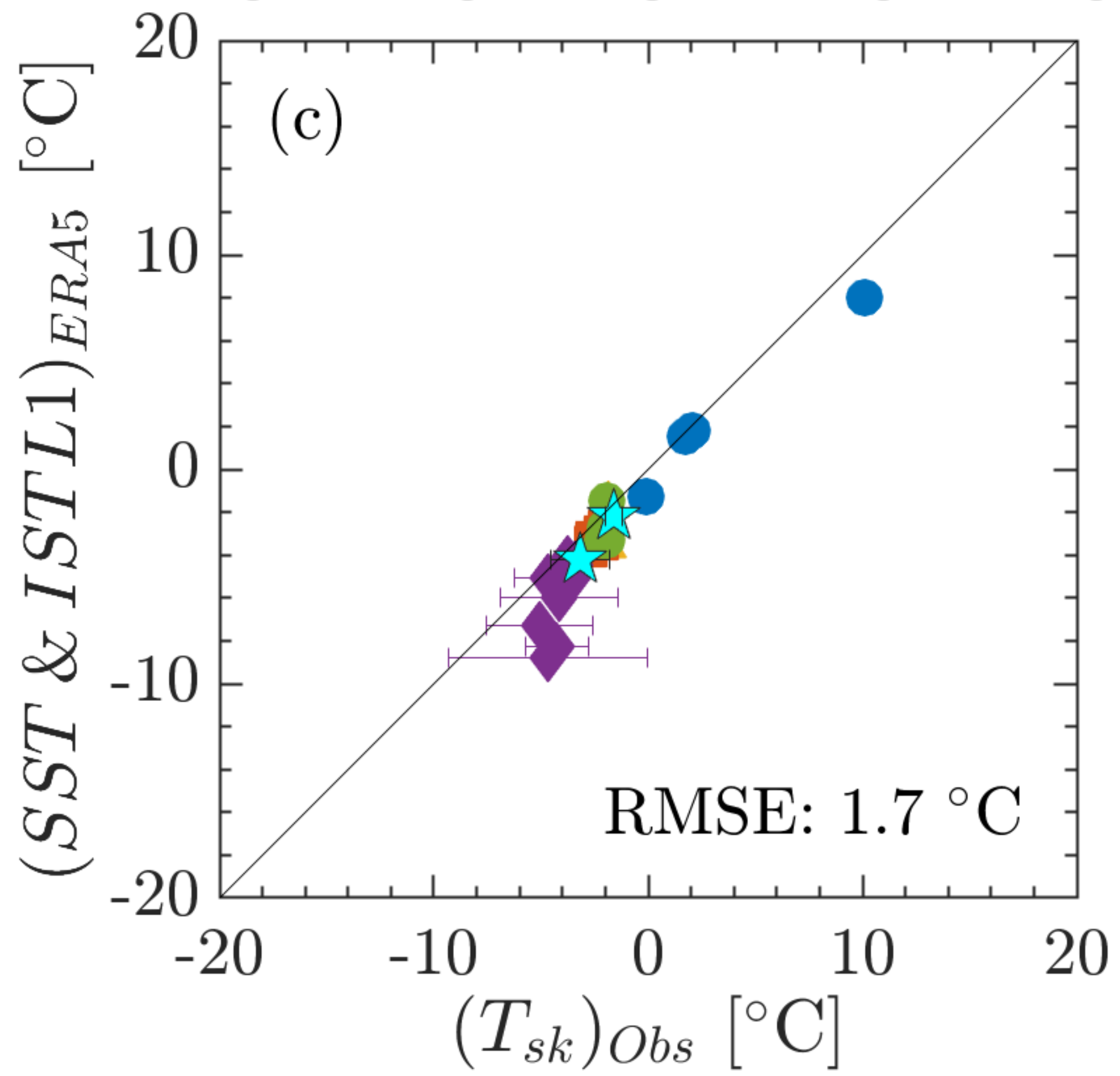
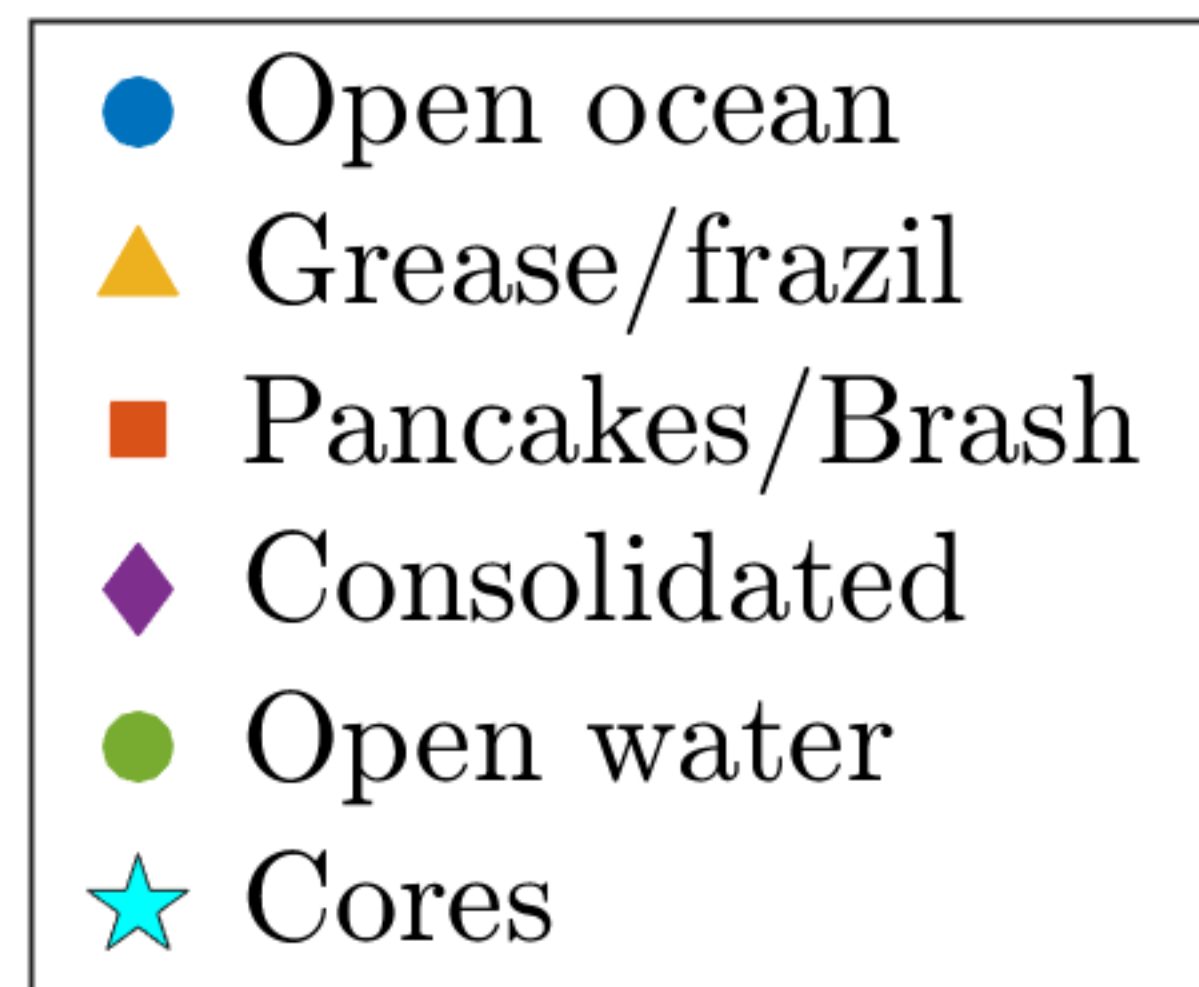
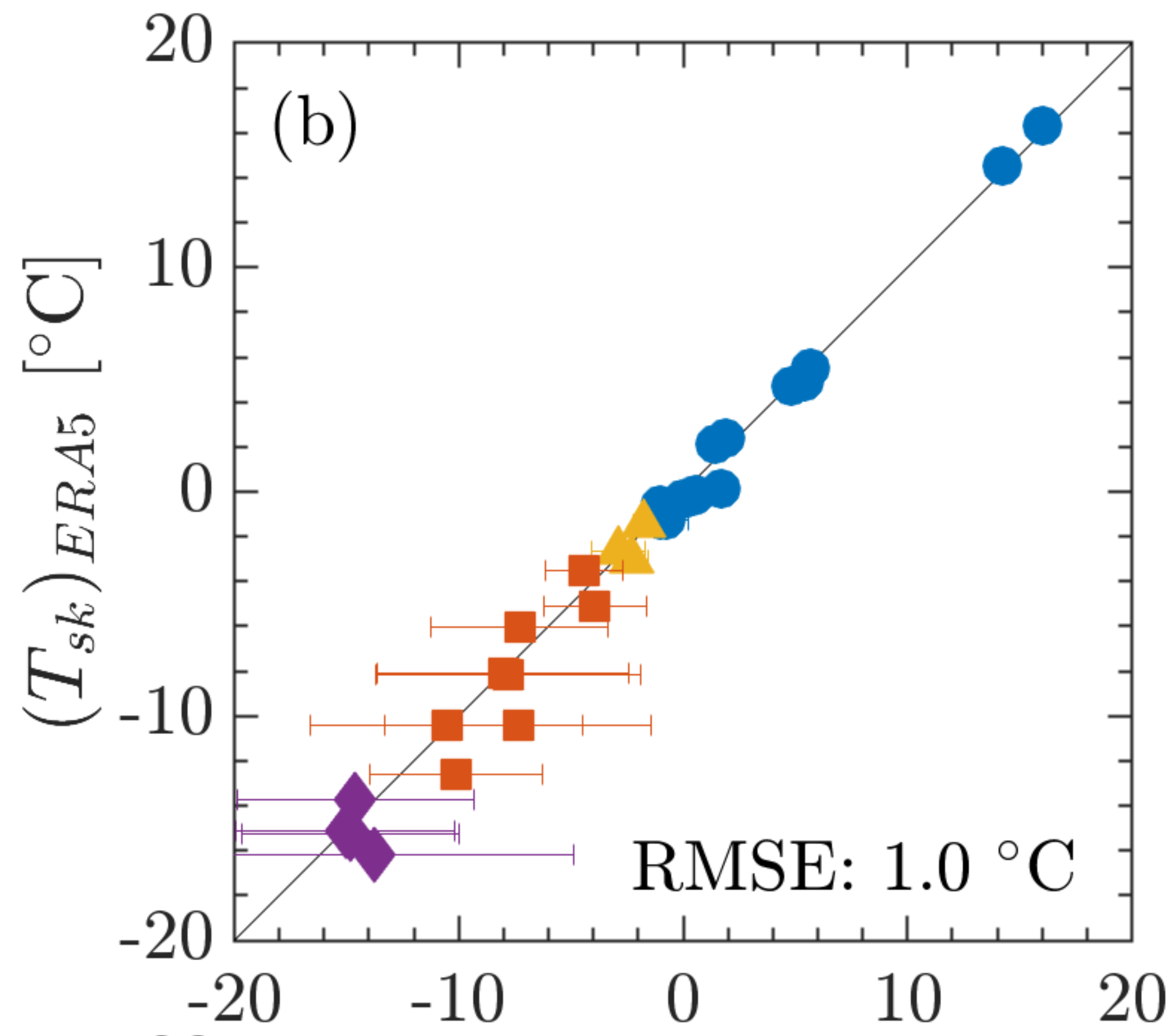
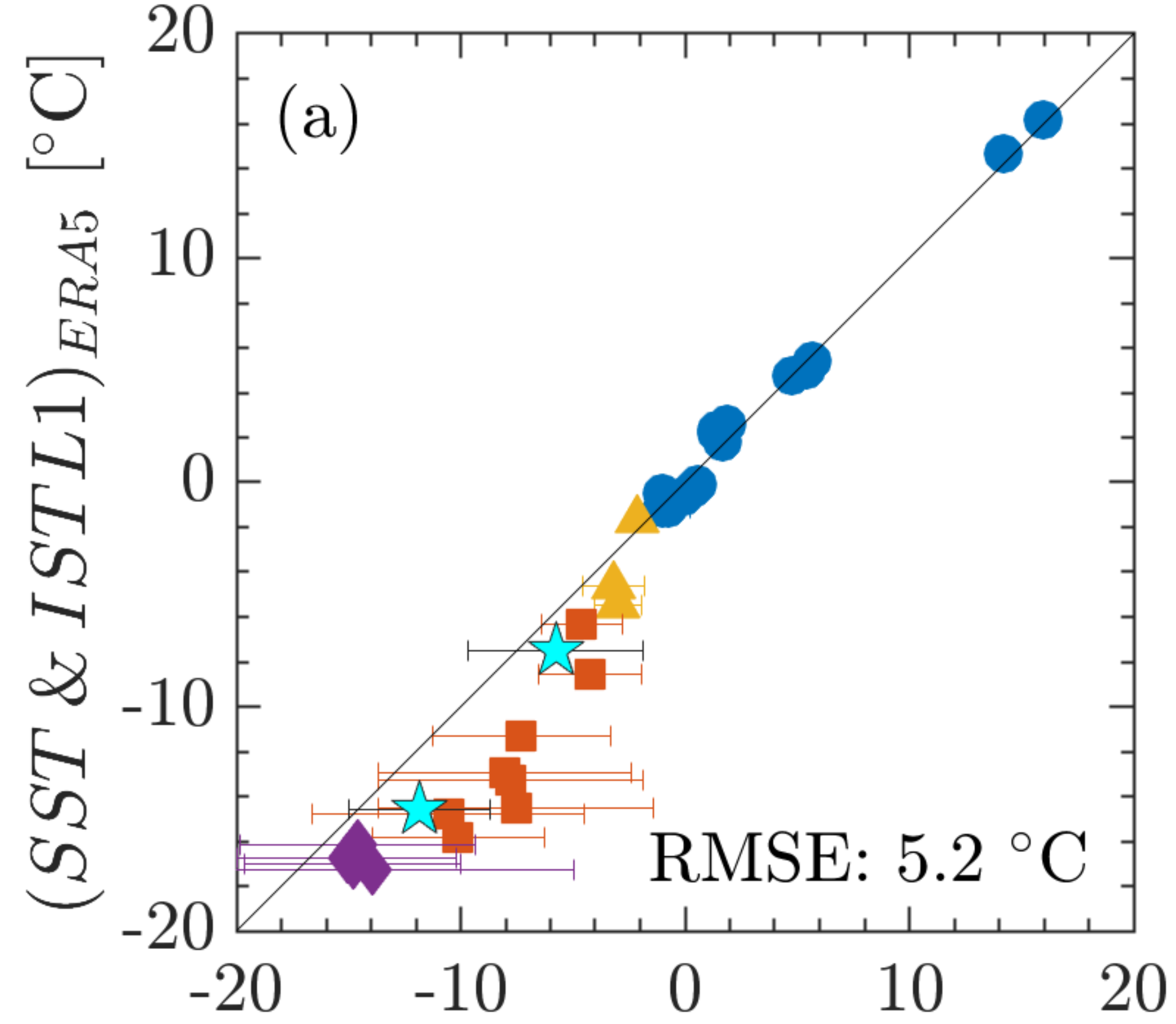


Figure 8.

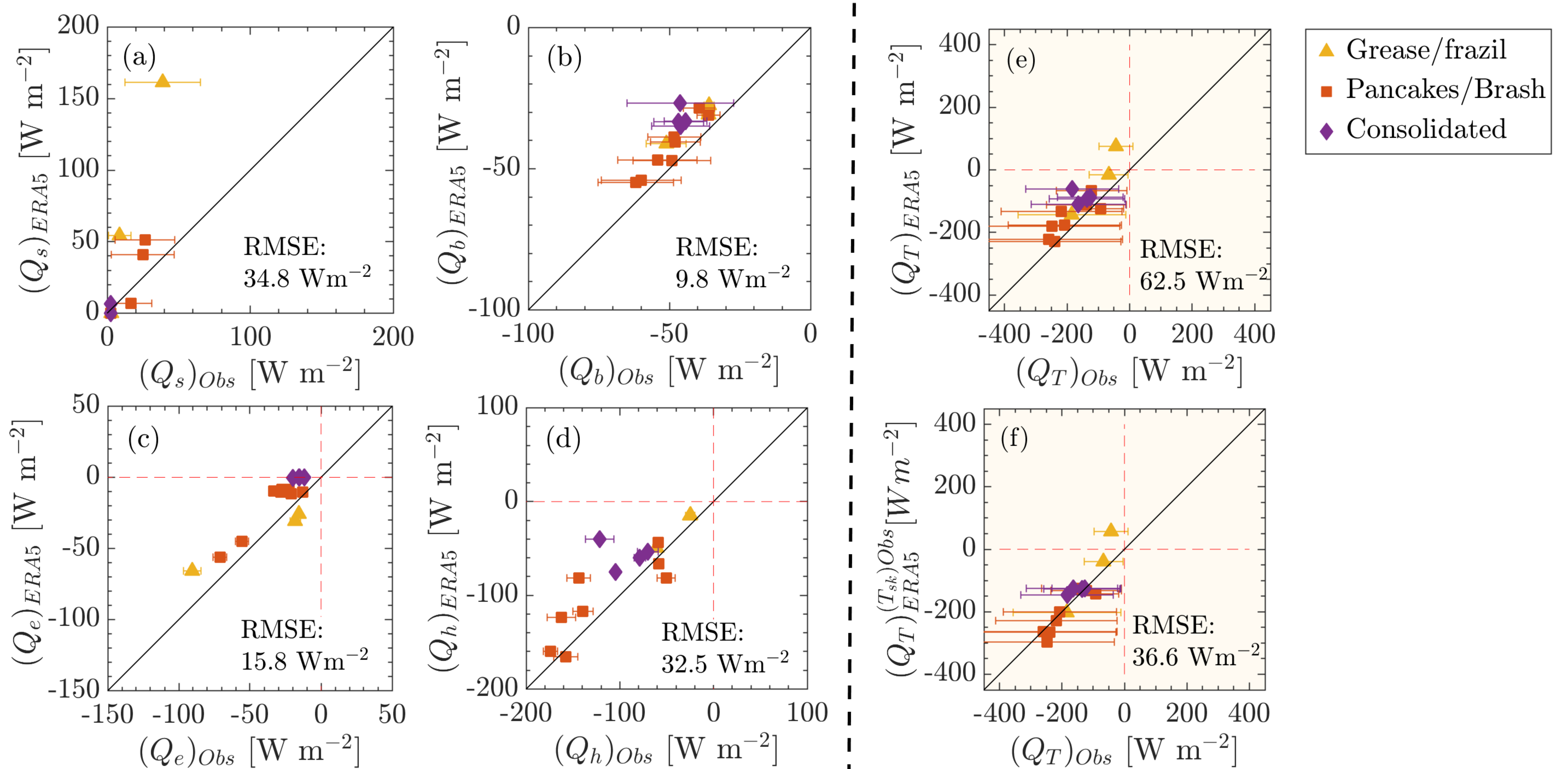


Figure 9.

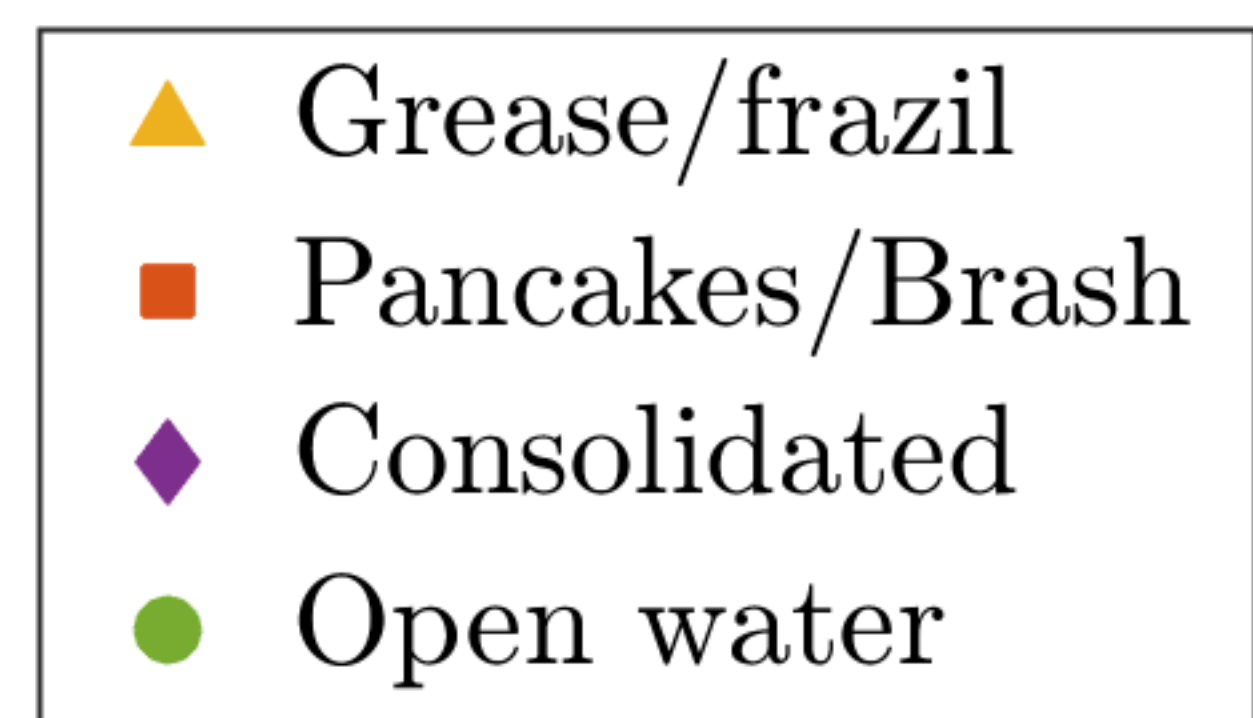
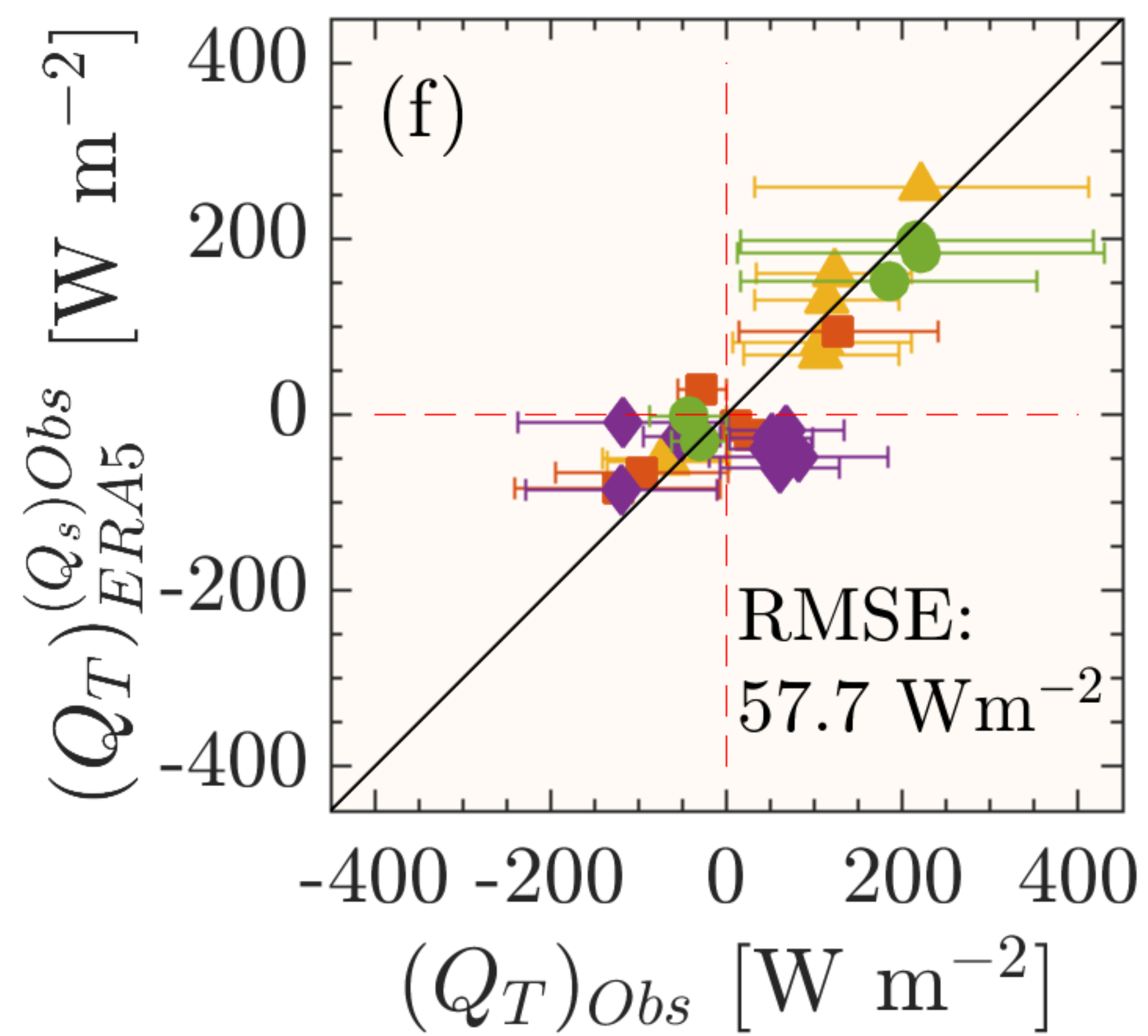
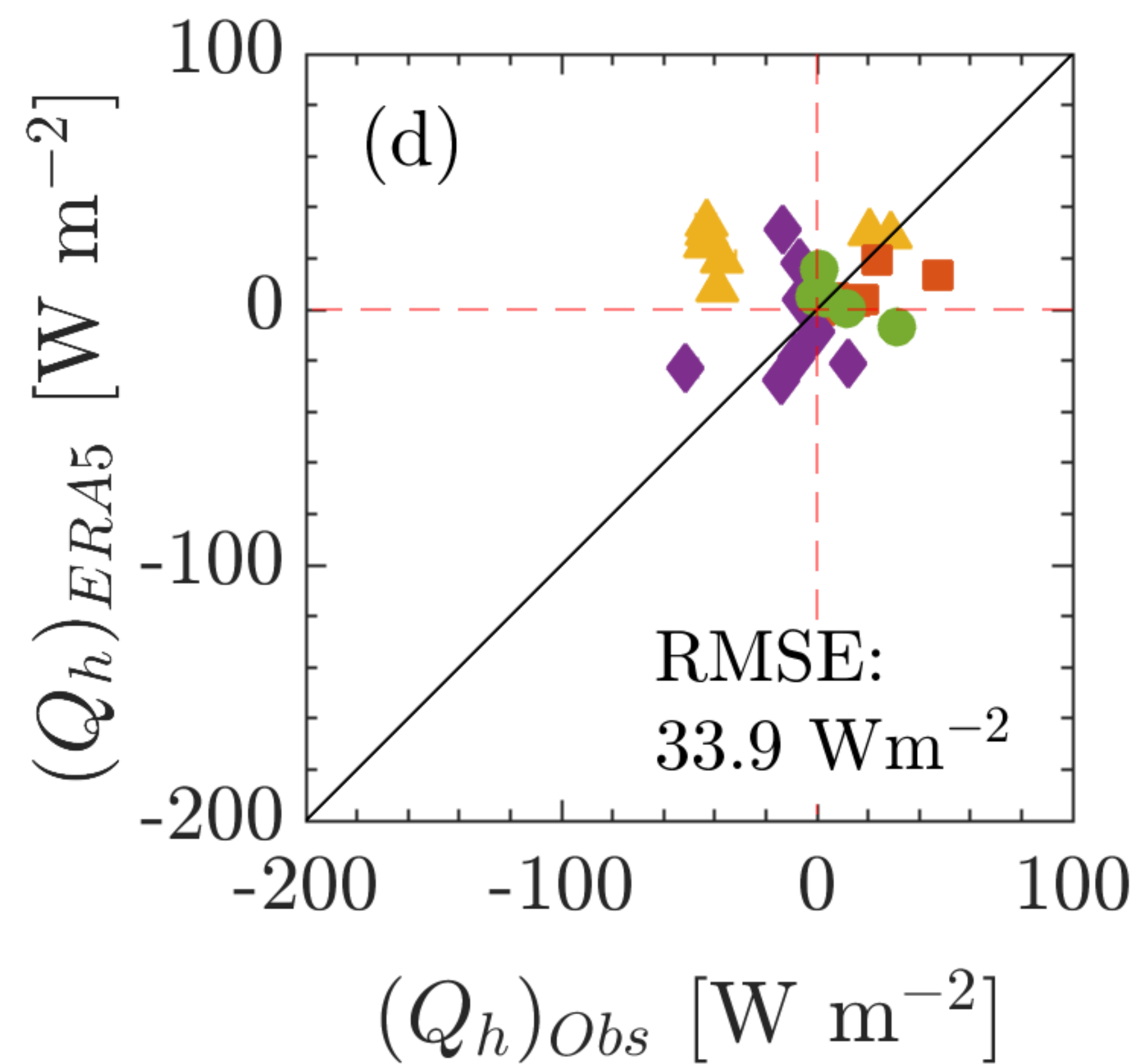
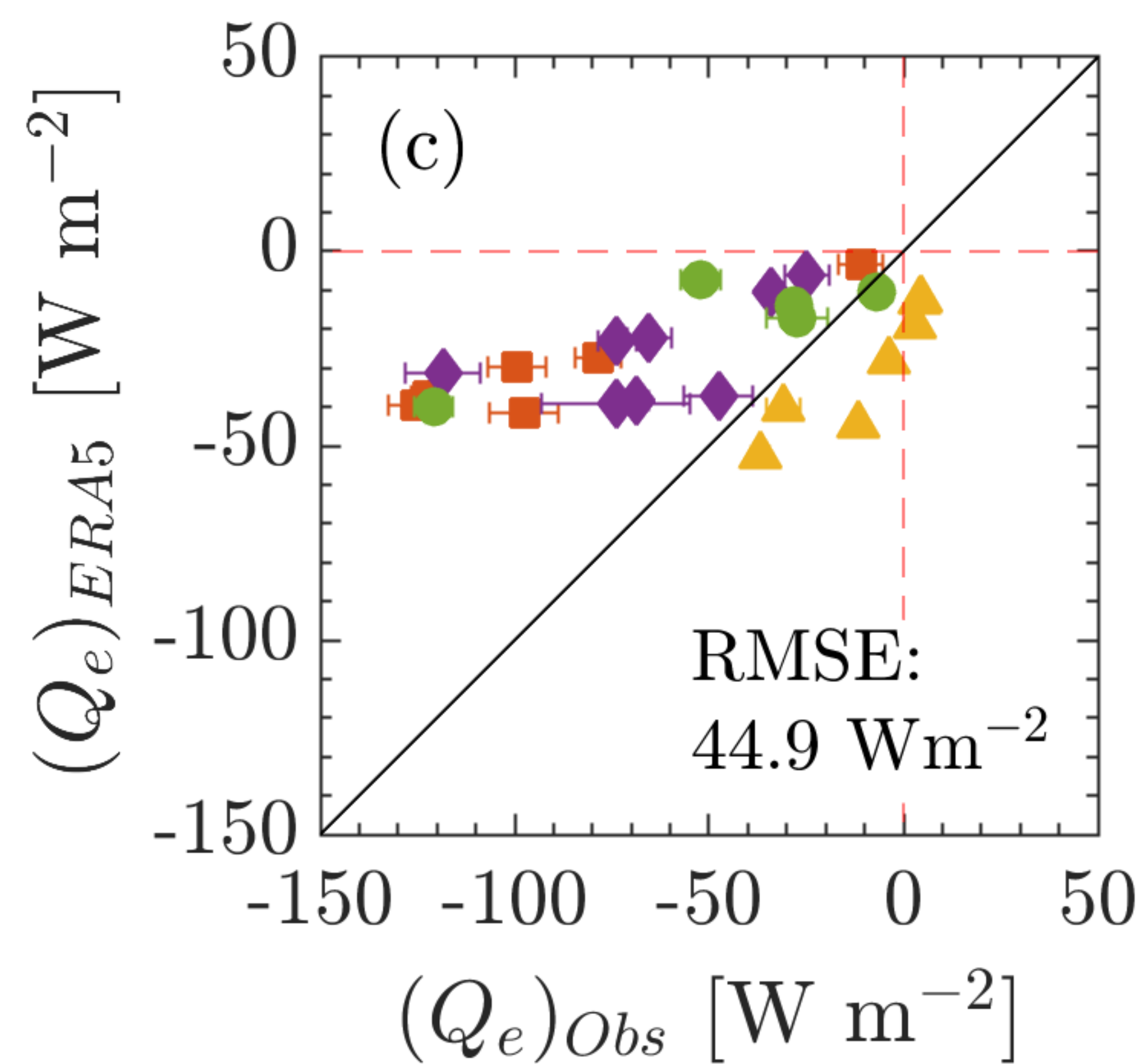
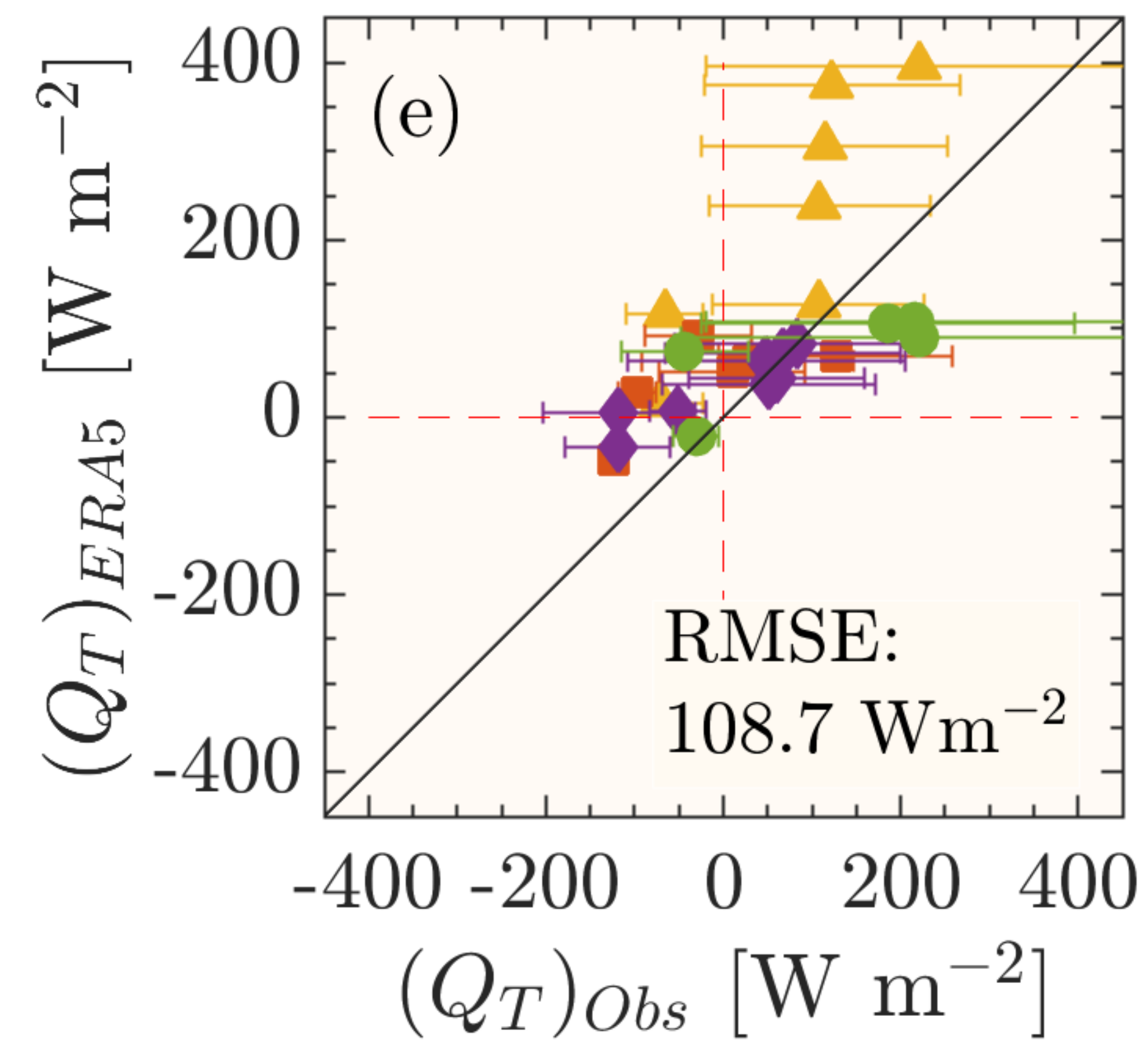
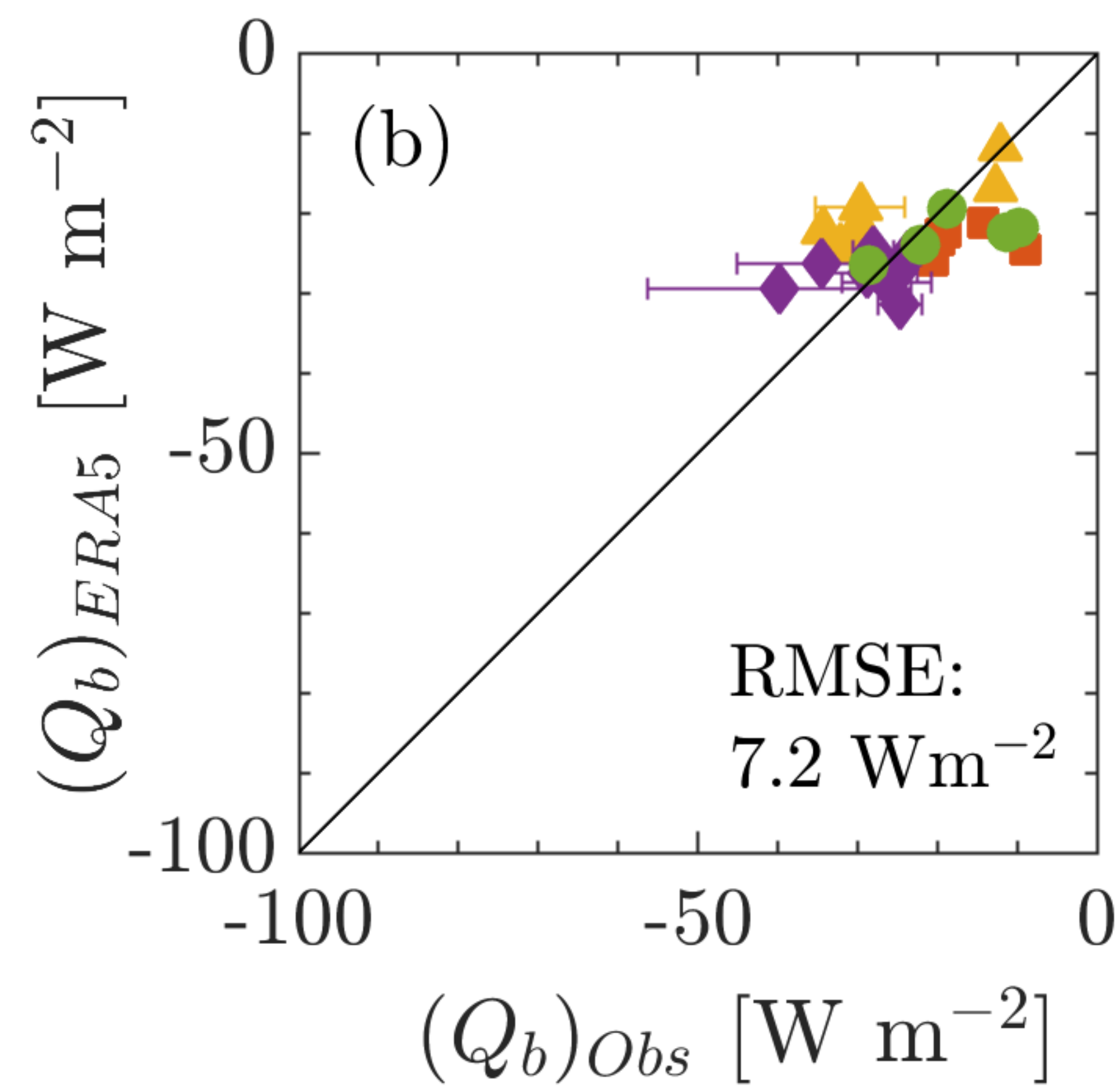
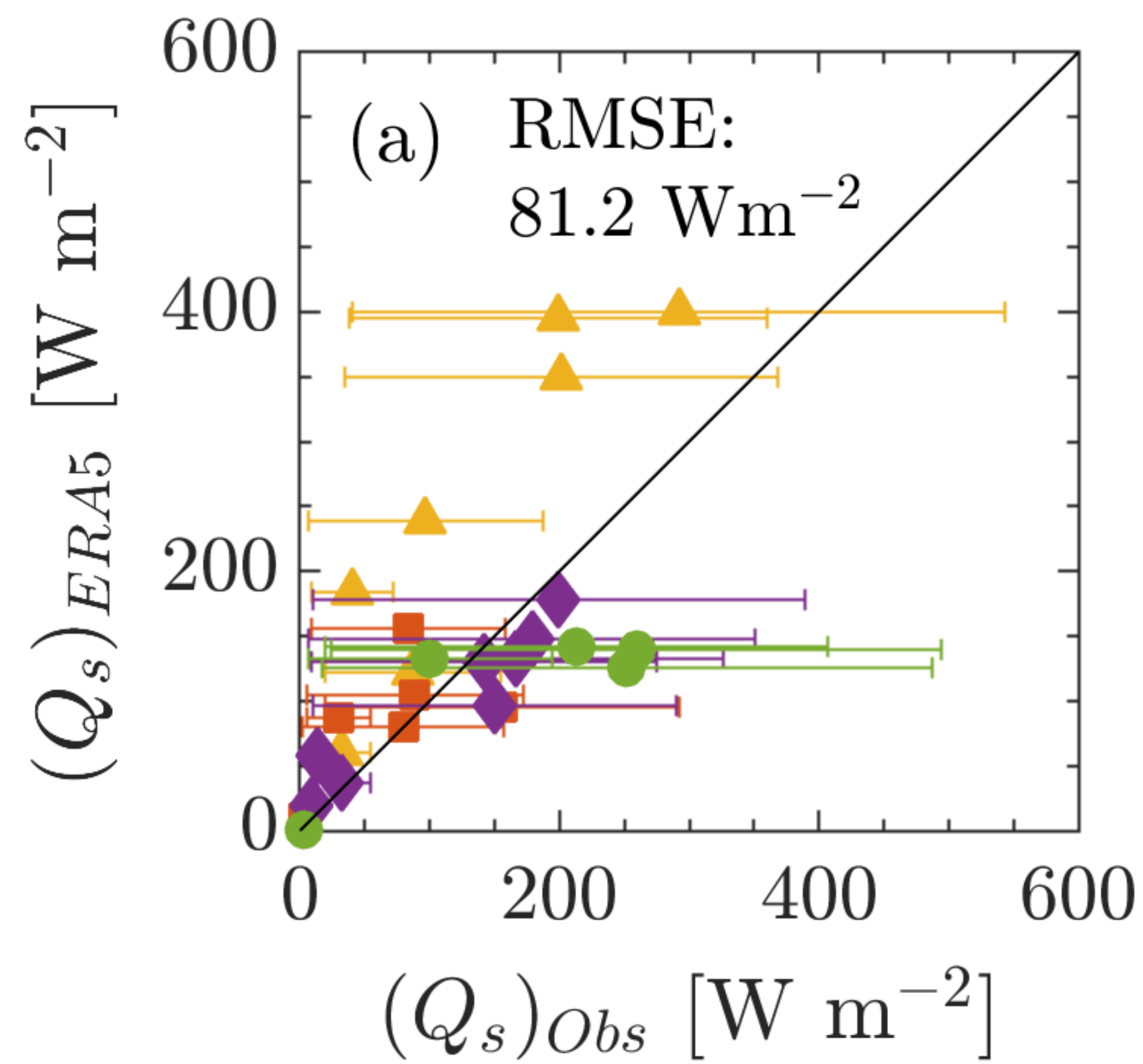


Figure A1.

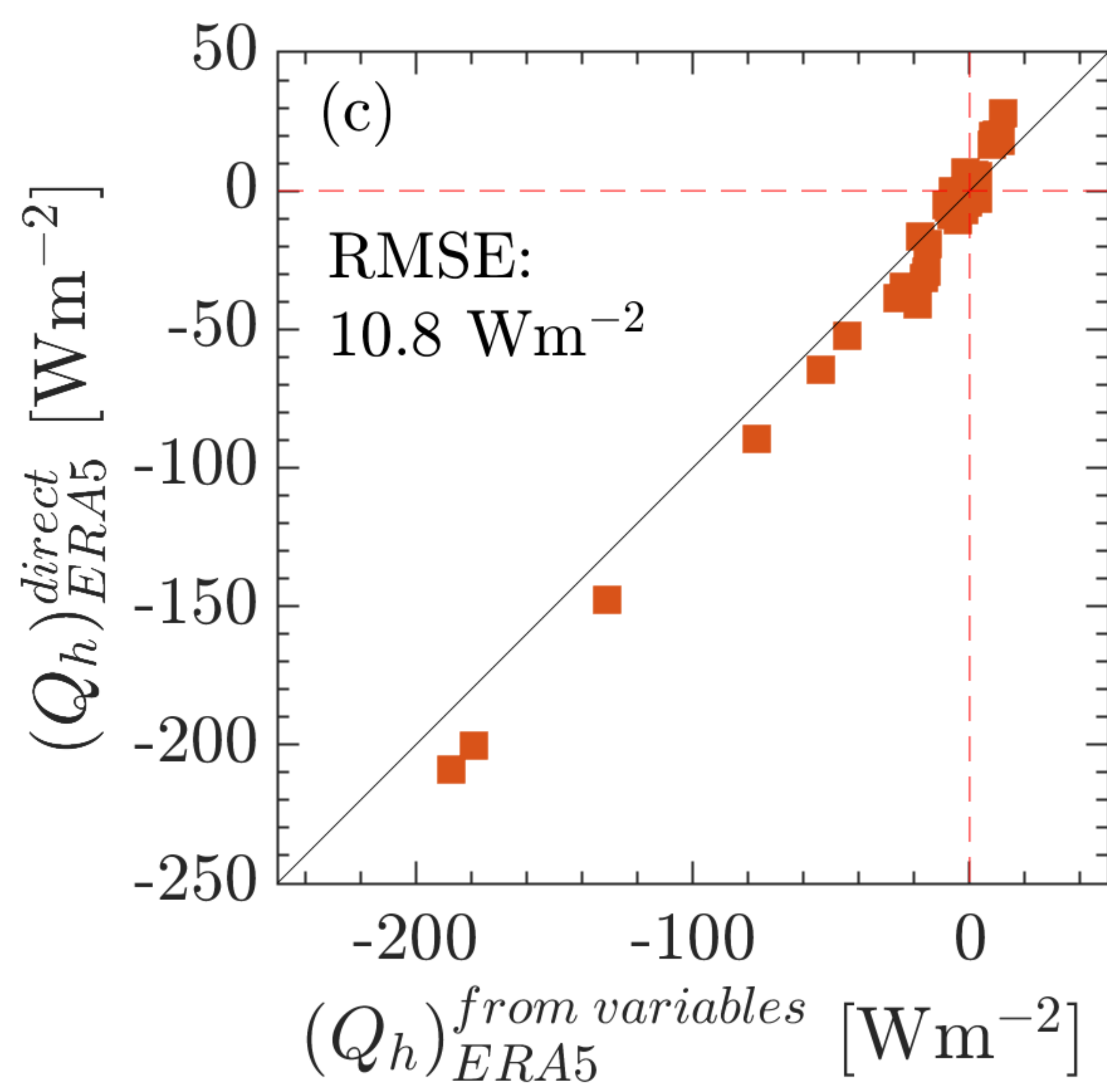
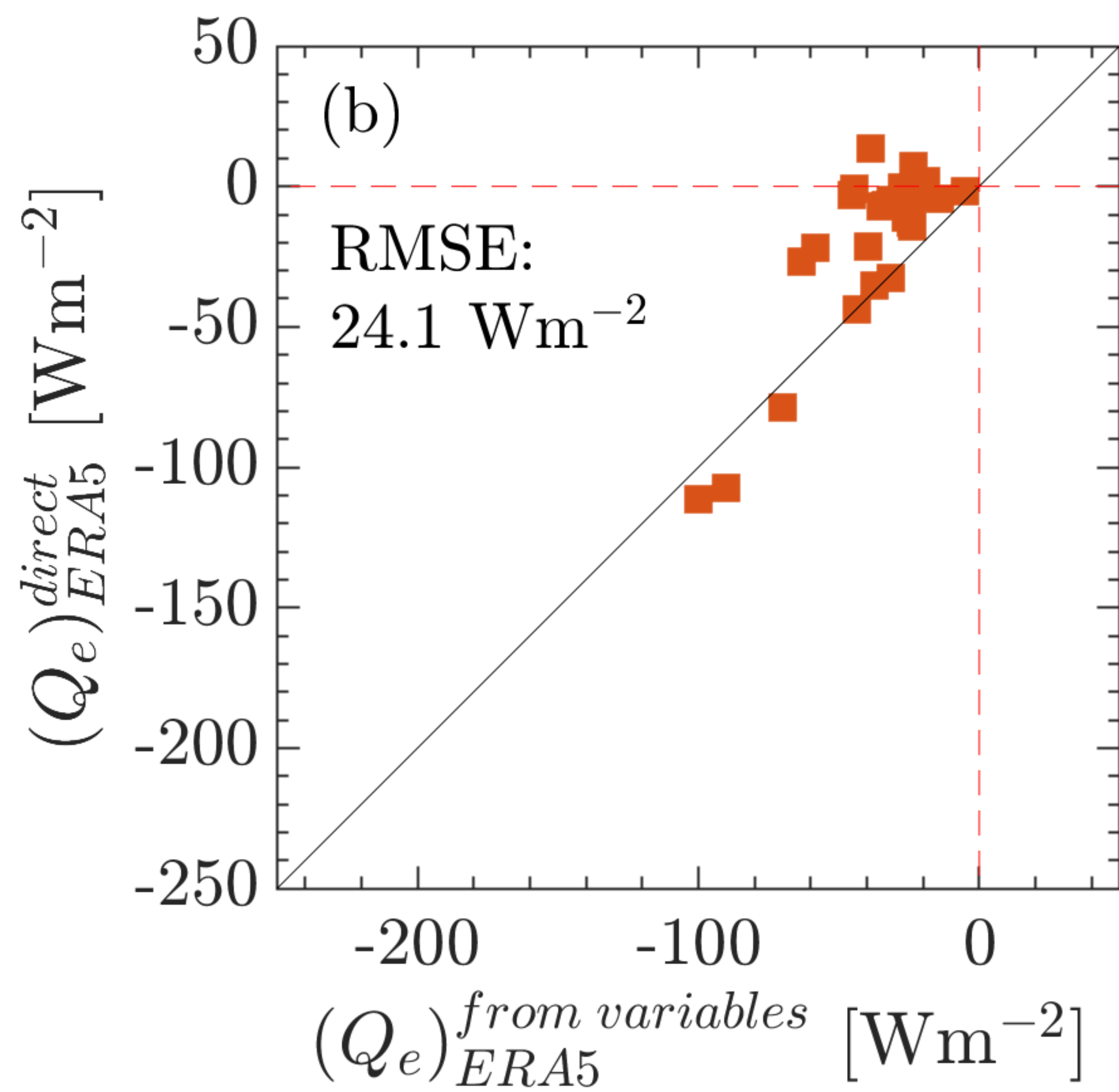
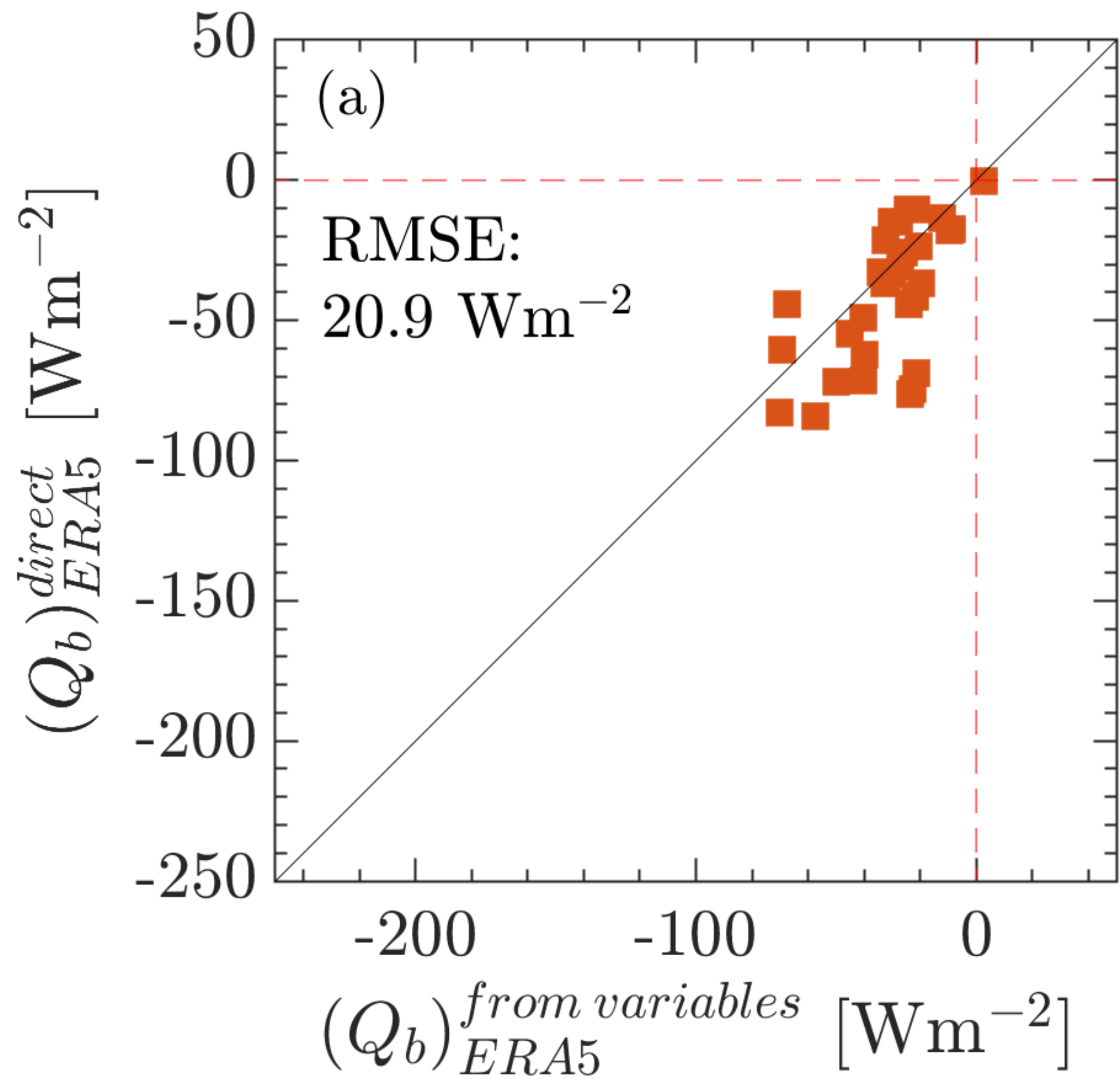


Figure B1.

